Forschungszentrum Karlsruhe
Technik und Umwelt

Wissenschaftliche Berichte
FZKA 5562

Application of Photothermal Methods for Environmental Studies: Copper Corrosion Layer (Patina)

A. Salnick, W. Faubel

Institut für Radiochemie
Projekt Mikrosystemtechnik

Februar 1995

Forschungszentrum Karlsruhe
Technik und Umwelt

Wissenschaftliche Berichte
FZKA 5562

Application of Photothermal Methods for Environmental Studies: Copper Corrosion Layer (Patina)

Alex Salnick and Werner Faubel

Institut für Radiochemie
Projekt Mikrosystemtechnik

Forschungszentrum Karlsruhe GmbH, Karlsruhe
1995

Forschungszentrum Karlsruhe GmbH
Postfach 3640, 76021 Karlsruhe

ISSN 0947-8620

Summary

Application of Photothermal Methods for Environmental Studies: Copper Corrosion Layer (Patina)

This paper describes the results of the application of modern nondestructive photothermal and photoacoustic methods to study one of the important environmental samples - copper protective corrosion layer (patina). Two different experimental techniques were used for these purposes: the photothermal beam deflection (PBD) method and Fourier transform infrared photoacoustic spectroscopy (FT-IR PAS).

A new photothermal approach in the studies of patinated copper layers was proposed. A noncontact and nondestructive PBD method was used for the characterization of thermal properties of patinated copper samples from the roof of the Stockholm City Hall. Quantitative measurements of thermal diffusivity and layer thickness performed on both the outdoor and indoor sides of patinated samples show a significant difference in their thermal properties. Photothermal images obtained for both sides of patinated samples were used for the analysis of patina layer surface morphology and the microstructure of includings.

The FT-IR PAS has proved to be a useful tool for nondestructive testing of the patina. By using this method we have identified about 10 different patina components including some new components such as copper (II) fluoride CuF_2xH_2O which have been not detected previously in the patina. The depth profiling capability of the FT-IR PAS method allowed us to determine the degree of photoacoustic saturation of the spectral bands and the depth distribution of the patina components. A new power index method was proposed for these purposes.

Based on the results obtained we concluded that photothermal methods are very useful experimental techniques allowing to obtain important quantitative information in such studies. These methods thus compare favourably with more common approaches of environmental samples examination which are usually more expensive, destructive and require special sample preparation.

Zusammenfassung

Anwendung von Photothermischen Methoden für Umweltuntersuchungen: Korrosionsschicht von Kupfer (Patina)

Diese Arbeit beschreibt die Ergebnisse über die Anwendung der modernen zerstörungsfreien photothermischen und photoakustischen Methoden auf ein umweltrelevantes Beispiel - die schützende Korrosionsschicht von Kupfer (Patina)

Zu diesem Zweck wurden zwei experimentell unterschiedliche Methoden verwendet: die photothermische Ablenkungsspektroskopie (engl. photothermal beam deflection (PBD)) und Fourier-Transform-Infrarot-Photoakustische-Spektroskopie (FT-IR PAS).

Eine neue photothermische Methode zur Untersuchung der Korrosionsschichten von Kupfer (Patina) wurde vorgestellt. Zur Charakterisierung der thermischen Eigenschaften der patinierten Kupferproben vom Dach des Stockholmer Rathauses wurden berührungsfreie und zerstörungsfreie Methoden verwendet. Die an der Innenseite und Außenseite der verschiedenen Patina-Proben durchgeführten quantitativen Messungen der thermischen Diffusivität und der Schichtdicke zeigten deutliche Unterschiede in ihren thermischen Eigenschaften. Die von beiden Seiten der Patina-Proben erhaltenen photothermischen Abbildungen wurden in Bezug auf die Oberflächengestalt der Patinaschicht und auf die Mikrostruktur von Einschlüssen untersucht.

FT-IR PAS hat sich dabei als ein sehr nützliches Instrument für zerstörungsfreie Untersuchungen der Patina erwiesen. Mit Hilfe dieser Methode konnten wir ca. 10 verschiedene Bestandteile, einschließlich einiger neuer Verbindungen wie Kupfer(II)-fluorid CuF_2xH_2O, die zuvor in der Patina nicht nachgewiesen werden konnten, identifizieren. Die Tiefendarstellungsmöglichkeit des FT-IR PAS erlaubt es uns einerseits den Grad der photoakustischen Durchdringung der Spektralbanden und andererseits die Tiefenverteilung der verschiedenen Patina-Bestandteilen zu bestimmen. Für diese Zwecke wurde eine neue „power index"- Methode vorgeschlagen.

Аннотация

Применение фототепловых методов в исследовавниях окружающей среды : слой медной коррозии (патина)

В настоящей работе приведены результаты применения современных фототепловых и фотоакустических методов к исследованию одного из важных объектов - защитного коррозийного слоя на меди (патины). Для этих целей были использованы два различных экспериментальных метода: фотодефлекционный (ФД) метод и метод фотоакустической Фурье-спектроскопии (Фурье-ФАС).

Предложен новый фототепловой подход в исследованиях патинированных слоев меди. Бесконтактный и неразрушаюший ФД метод был использован для определения тепловых свойств патинированных образцов с крыши Стокгольмской Ратуши. Количественные измерения коэффициента тепловой диффузии и толщины слоя, проведенные как на внешней, так и на внутренней сторонах патинированных образцов, показали значительные отличия в их тепловых свойствах. Фототепловые изображения, полученные для обеих сторон патинированных образцов, были использованы для исследования морфологии поверхности слоя патины и микроструктуры включений.

Показано, что метод Фурье-ФАС является удобным средством неразрушающего тестирования патины. Используя этот метод, мы идентифицировали около 10 различных компонентов патины, включая некоторые новые компоненты, такие как флюорид меди CuF_2xH_2O, который ранее не обнаруживался в патине. Способность ФД метода проводить профильный анализ по глубине образца позволила нам определить степень фотоакустического насыщения спектральных линий и распределение компонентов патины по глубине. Для этих целей предложен новый степенной метод.

Основываясь на полученных результатах, мы пришли к заключению, что фототепловые методы являются весьма удобным экспериментальным средством, позволяющим получать важную информацию в таких исследованиях. Эти методы выгодно отличаются от более известных подходов к исследованию окружающей среды, которые обычно являются более дорогими, разрушающими и требующими специальной подготовки образцов.

Contents

Chapter 1
Photothermal Nondestructive Evaluation of the Patina

Introduction

It is well known that copper when exposed to the atmosphere, forms a thin layer of corrosion which is commonly green or greenish-blue. This protective patina layer is generally regarded as an aesthetically pleasing as well as a protective coating of the copper substrate. Its colour indicates that the architecture object or sculpture has been around for a long time, for it takes many years to form a sufficiently thick green patina layer.

The changing environment has accelerated the processes of degradation of patina formerly characterized by great durability. Since the thirties of this century the problem of scientific analysis of patina and its conservation became of great importance.

The first contribution to a scientific understanding of the patina phenomenon has been made by Vernon [1] who performed many experiments on various patinas and defined its main chemical components. Recently, Mattsson [2], Weil et al. [3], Graedel and co-workers [4-11] and Livingston [12] have published results of detailed studies of different patinated samples using modern analytical techniques. They have identified a number of new components of copper patinas and deduced the mechanisms of patination and patina degradation processes.

Copper patinas are chemically and physically complex structures. A number of powerful analytical methods, such as metallography [5], X-ray diffraction [6], evolved gas analysis [6], X-ray photoelectron and Auger electron spectroscopy [7,13], chromatographic methods [8] and other techniques are usually applied for patina examination. Most of these methods are capable of obtaining different kinds of chemical and mineralogical data rather than information about macro-physical properties of patina. In addition, they are usually expensive and can be used only under laboratory conditions.

On the other hand, there is a great interest in studying the physical properties of patinas and in developing new non-expensive and non-destructive techniques which could be applied for in-field measurements and first control of natural and artificial protective layers like patina.

One of the possible solutions for this problem could be the photothermal approach. The initial observation of the photothermal effect in solids by Bell [14] was based on the production of audible sound by the periodic interruption of a beam of light. The revival of photothermal methods for studies of solids was the result of work by Rosencwaig [15] who developed analytical methods and applications specific for solids. Modern photothermal science includes more than 15 methods which differ in the detection principles and are used successfully to study solids, liquids and gases [16]. In particular, these methods are very efficient in quantitative nondestructive evaluation, microscopy and spectroscopic studies of materials [17-18].

As a first step in such a photothermal approach we describe in Chapters 1 and 2 of the present work the results of application of the relatively new nondestructive and noncontact Photothermal Beam Deflection (PBD) method [19-21] (also known as „Mirage detection" technique) for the characterization of thermal properties of patinated copper samples. The data result from quantitative nondestructive measurements of photothermal parameters of patina and photothermal imaging of both outdoor and indoor sides of samples from the roof of the Stockholm City Hall.

We also discuss some characteristic features in the application of the PBD method to such an analysis as well as the ways of further development of the photothermal approach in patina studies.

1.1 The PBD Method Physical Principles

1.1.1 General

After the first observations of the Mirage effect by Knyazev and co-workers [19] the PBD investigation method based on this effect was reintroduced by Boccara et al. [20] and Aamodt and Murphy [21]. Variants of this technique are used in a wide range of spectroscopic and imaging applications. A schematic diagram of the physical principle of the PBD method is shown in Fig.1.

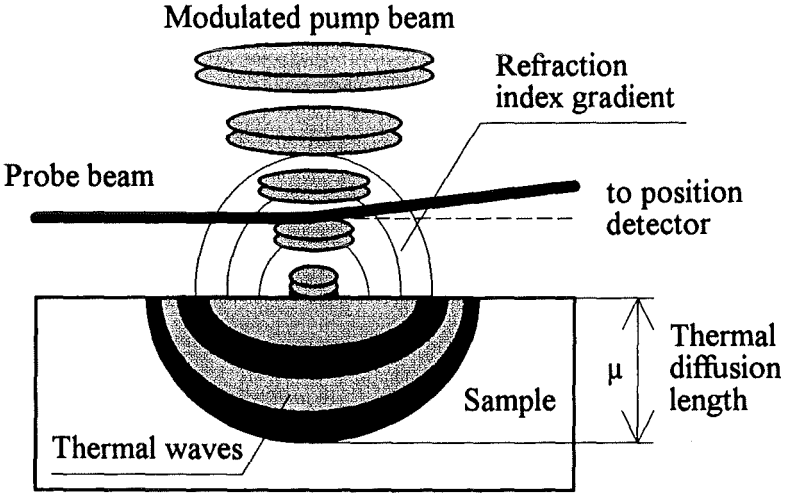

Fig.1 Schematic diagram of the physical principle of the PBD method.

The periodic heating of the sample by a modulated pump beam produces periodic heating of the gas (air) adjacent to the sample surface due to the heat transfer from the sample. This causes periodic variations in the index of refraction, n, of air. This temperature dependent density oscillation in the air is locally monitored with a probe laser beam (focused onto the heating region) which skims along the surface of the sample and through the heated region.

Periodic deflections of this probe beam due to the refractive index gradient are measured by a position sensitive optical detector. Hence the detection is made over a line along the path defined by the illuminated region of the surface. The deflection angle Φ with respect to the original trajectory is given by [21]:

$$\Phi = - \int_P (1/n)(dn/dT) \nabla T_g \times dl \qquad (1)$$

where dn/dT is the temperature gradient of the index of refraction, T_g is the periodic temperature distribution in the air, P is the probe beam path, and dl is an incremental distance along P.

In most cases this deflection is not larger than a few milliradians. Since the temperature changes involved are small, dn/ndT is usually assumed to be constant and can be taken out of the integral. The deflection Φ can be resolved into two components, Φ_n normal to the sample surface and Φ_t parallel to the sample surface.

It has been shown [21] that when measurements are made close to the sample surface:

$$\Phi_n \propto \text{weighted mean value of T along P} \qquad (2)$$

$$\Phi_t \propto \text{weighted mean value of } (\partial T/\partial y) \text{ along P} \qquad (3)$$

Since the normal component Φ_n is sensitive to the surface temperature, it shows thermal discontinuities such as coatings, delaminations and inclusions that have lateral dimensions large enough to perturb the heat propagation into the material perpendicular to the surface [22]. The transverse component Φ_t is sensitive to the lateral heat flow indicating vertical or near vertical thermal boundaries such as cracks and crack-like features.

1.1.2 Depth profiling

One of the main advantages of the PBD method is the possibility of varying the sampling depth. The thermal wave amplitude into the sample decays rapidly with depth, and over a distance μ (called the thermal diffusion length) it is reduced to e^{-1} of its initial value (Fig.1).

This distance is defined as:

$$\mu = (\alpha/\pi f)^{1/2} \tag{4}$$

where α is the sample thermal diffusivity ($\alpha = \kappa/\rho c$, where κ, ρ and c are the sample thermal conductivity, density and heat capacity, respectively) and f is the modulation frequency of the pump laser beam.

This thermal diffusion length depends on both material properties and modulation frequencies, and it is roughly the penetration depth of thermal waves into the sample. Therefore, the PBD method is a near-surface technique where the depth range can be adjusted via the laser modulation frequency, thus allowing for depth profiling.

1.2 Experimental Set Up and Samples

1.2.1 Set up

A block-scheme of the PBD experimental set up, which is similar to that usually used in such studies [23], is shown in Fig.2.

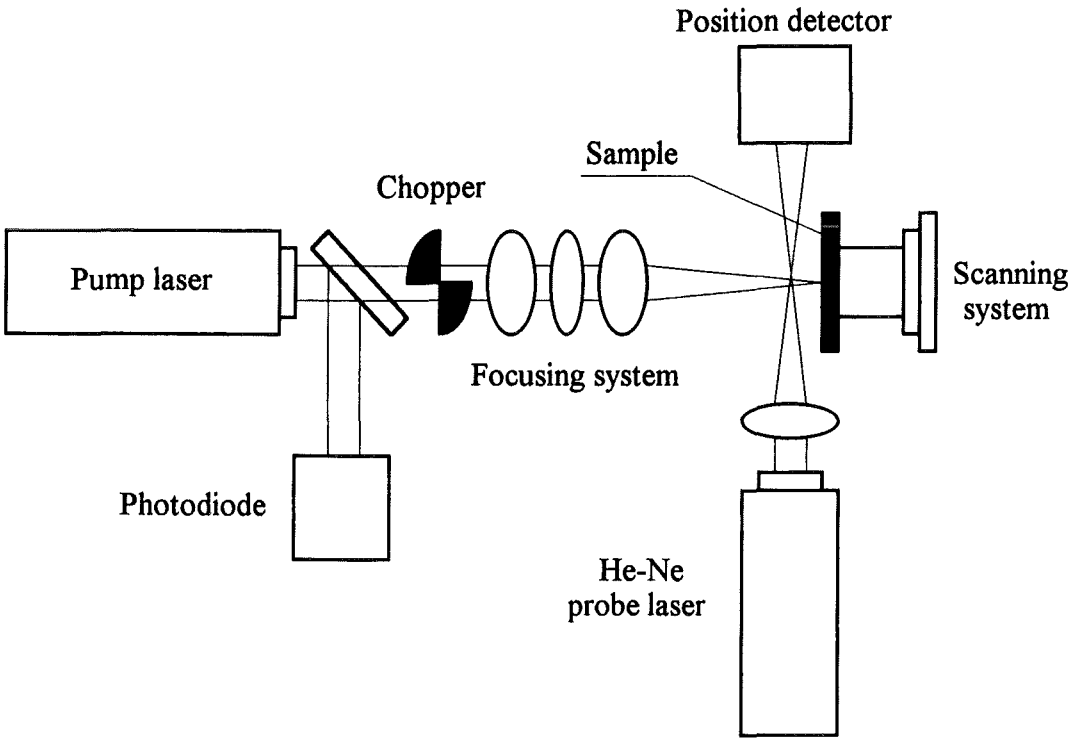

Fig.2 Schematic diagram of the experimental set up of the PBD method.

Three different lasers: Nd:YAG (wavelength λ=1064 nm, attenuated to 10 mW insensity, ADLAS Model DPY321, Luebeck, Germany), He-Ne (λ=633 nm, 10 mW, UNIPHASE Model 1096, Mantea, CA) and Nd:YAG frequency-doubled (λ=532 nm, 10 mW, ADLAS Model DPY315II, Luebeck, Germany) have been used as pumping sources. The pump beam was modulated by a mechanical chopper (from 10 Hz up to 10 kHz) and has been focused onto the sample surface by means of optical components.

A He-Ne laser (λ=633 nm) has been used as a probe beam source [24]. The probe beam deflection signal (both normal Φ_n, and transverse Φ_t components) has been detected by a four-quadrant position detector and processed by means of a lock-in amplifier.

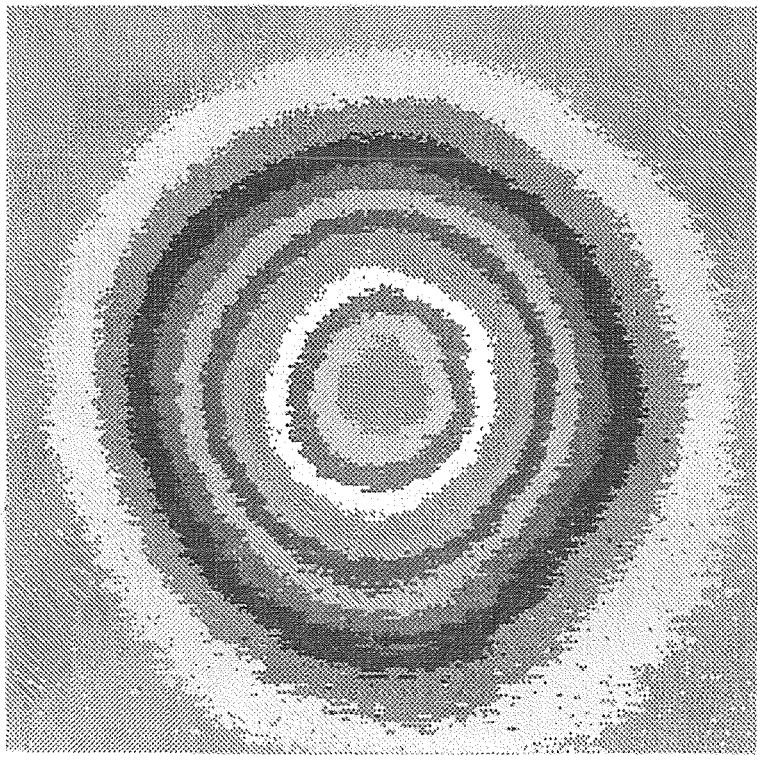

Fig. 3 A He-Ne probe beam profile obtained with the use of 5 μm diaphragm.

The pump and probe beams spatial profiles were measured with the use of simple system contains a scanning pinhole and photodiode. Figures 3 and 4 present the profiles for a He-Ne probe beam and a Nd:YAG (λ=1064 nm) pump beam. The probe and pump beams radii have been evaluated to be about 60 μm and 100 μm, respectively. These characteristic dimensions were varied for the photothermal imaging (Chapter 2) between 30 and 200 μm by changing the focusing conditions.

The pump beam intensity has been controlled by a photodiode. A scanning system allowed to move the sample to within 0.5 μm accuracy to obtain the photothermal images.

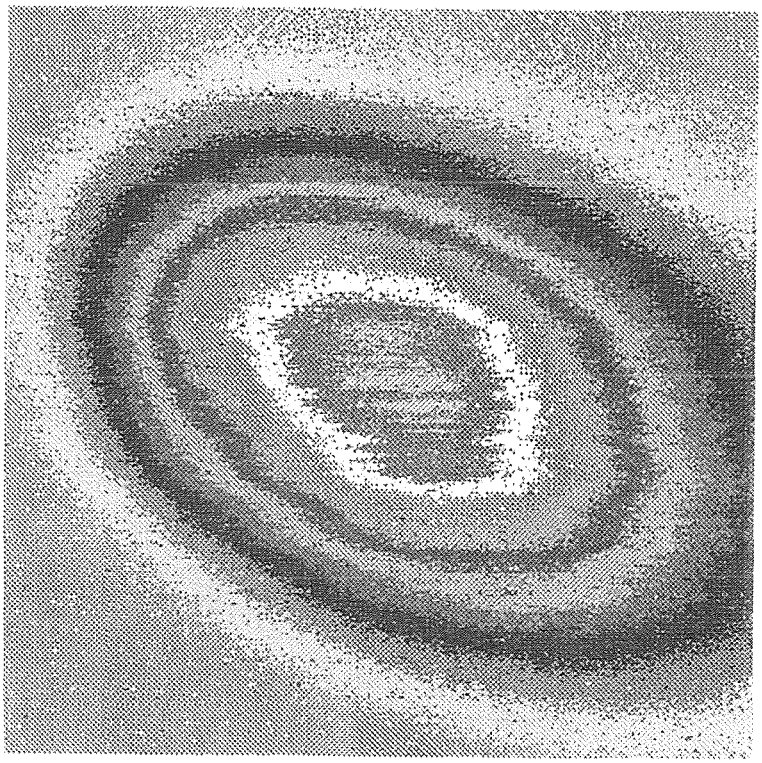

Fig. 4 A Nd:YAG (λ=1064 nm) pump beam profile obtained with the use of 5 μm diaphragm.

1.2.2 Samples

The samples of ca. 600 μm thickness and of 10x10 mm^2 dimensions cut from a piece of the roof of the Stockholm City Hall have been examined without any additional pre-treatment. The exposure time of the samples to the atmosphere was approximately 65 years [13].

Each sample had two patinated surfaces: a green outdoor side (which had been exposed to the atmosphere) and a brown indoor side as shown in Figs. 5(a) and 5(b). The green colour of the outdoor side of the samples is due to the presence of brochantite $Cu_4(OH)_6SO_4$ which is almost always the main component of the patina [4].

The presence of brochantite at outdoor side of samples has been confirmed by means of the FT-IR Photoacoustic Spectroscopy (FT-IR PAS) [25]. A detailed PA spectroscopic analysis of the patina is presented in Chapter 3 of the present work.

It is also known [4,27-28] that natural copper patinas are spatially quite heterogeneous, and the surfaces show a highly porous structure. In addition, different kinds of atmospheric particles like aluminia, iron oxide, silica etc. are commonly incorporated into copper patinas [3,4] and can be clearly seen even in photomicrographs (Fig. 5(a)). The presence of very hard and strongly adherent small black spots on the surface of patina has been noted in previous studies [4,29].

Two samples, one having typical outdoor and indoor patina surfaces and another one containing the above mentioned black spots on the outdoor side have been chosen for analysis. They have been numbered as sample #1 and sample #2, respectively.

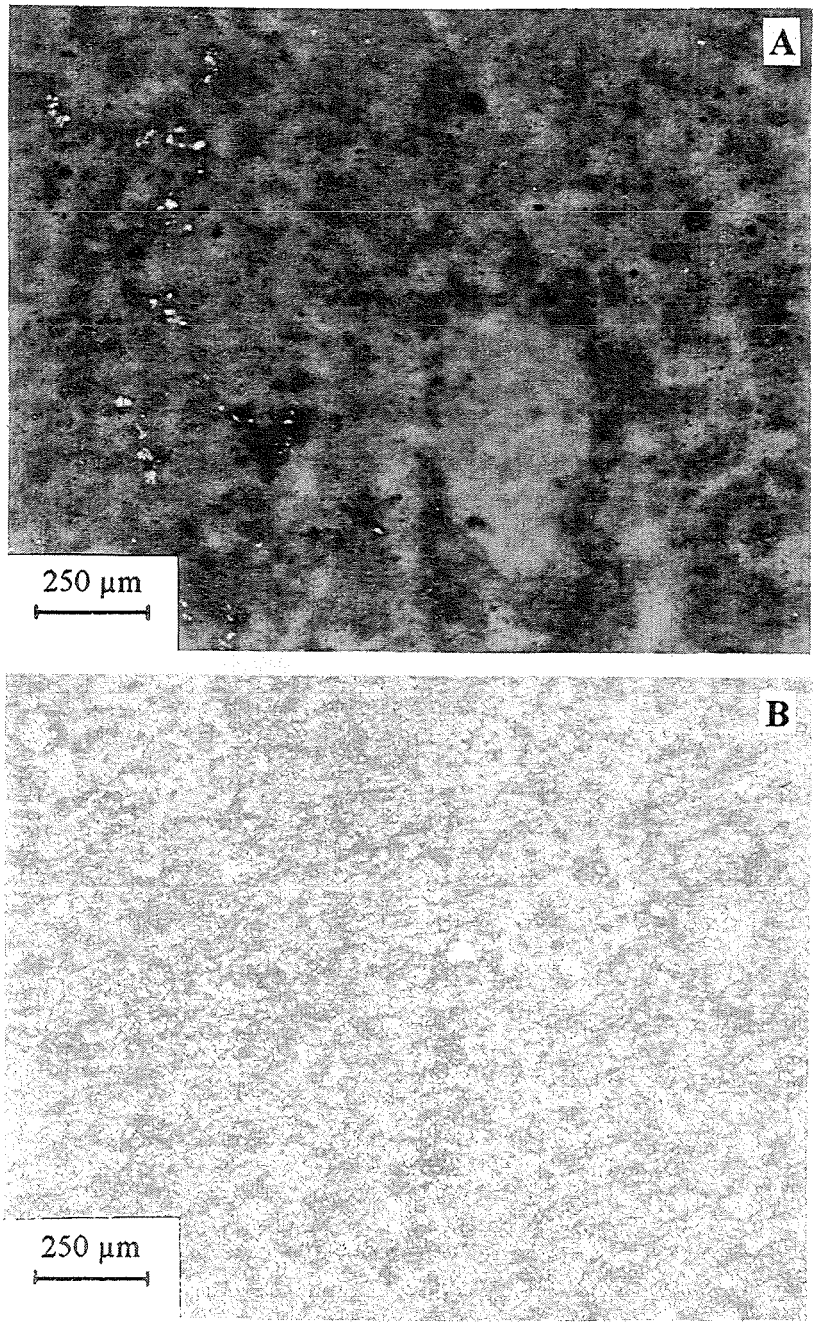

Fig.5 Microphotographs of outdoor (a) and indoor (b) surfaces of the patinated sample #1 taken in the central part of the sample.

1.3 Nondestructive Evaluation of Thermal Parameters

1.3.1 Zero crossing method for thermal diffusivity measurement

It has been shown above that measurements of the transverse component Φ_t of the PBD signal can provide a direct noncontact determination of the thermal diffusivity [30-33]. This is carried out by scanning the probe beam relative to the pump beam with a constant height from the sample surface. The so called zero crossing (ZC) method is applied to calculate the values of thermal diffusivity (Fig.6).

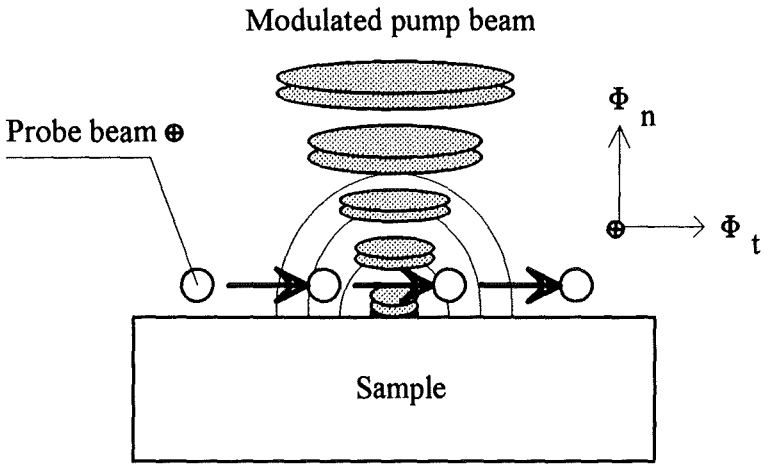

Fig.6 Schematic diagram of the zero-crossing method for thermal diffusivity measurement using the PBD technique.

This ZC of thermal diffusivity measurement is based on the linear relation between the first noncentral zero crossing d of the real part of the transverse component $Re(\Phi_t)$ against the inverse root of the modulation frequency $f^{-1/2}$ [31-32]. Each zero crossing corresponds to a phase shift of 90° with respect to the central zero. The slope of this straight line m gives the thermal diffusivity α via the relation [32]:

$$m = (\gamma\pi\alpha)^{1/2} \tag{5}$$

where γ is a parameter which depends on the bulk thermo-optical properties of the material.

This ZC method was applied to measure the thermal diffusivities of the outdoor and indoor patina layers of the samples. As an example, the PBD-transverse amplitude measured on the indoor side of sample #1 is plotted in Fig.7 against the pump-probe beam separation distance.

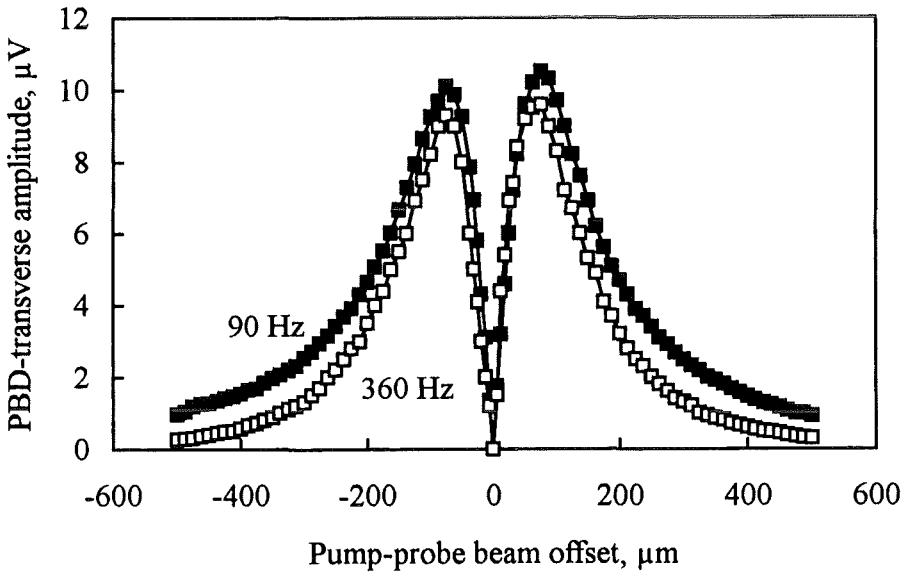

Fig.7 Experimental dependence of the PBD-transverse amplitude on the pump-probe beam offset for the indoor side of the patinated sample #1 at two modulation frequencies.

Here two peaks (which have their maxima at some distance from the central point) correspond to the deflection of the probe beam into two opposite directions. The first noncentral zero crossing *d* is obtained from the analogous dependence of the real part of the PBD-signal (Fig.8). The value of *d* decreases with increasing pump beam modulation frequency.

It should be pointed out that the first noncentral zero crossing of $Re(\Phi_t)$ as measured directly in the experiment (Fig.8) is not related to a phase shift of 90° due to the finite height of the probe beam above the sample surface (which is typically 100-200 μm). In this case the correction procedure proposed by Salazar et al. [33] should be applied.

1.3.2 Correction procedure

The points corresponding to a 90° phase difference (called true zero crossing) can be obtained by introducing a suitable phase shift in the Argand diagram (i.e. dependence of the $Re(\Phi_t)$ on $Im(\Phi_t)$) thus producing a rotation in the complex plane of the loops which keeps them in a vertical position (Fig.9). This correction procedure was applied to all measurements of the thermal diffusivities.

Another important problem in the determination of the thermal diffusivity appears in the case of low diffusivity materials such as the outdoor patina layer . If the thermal diffusivity of the sample is much lower than that of the gas ($\alpha = 0.19$ cm^2/s for the air), the applicability of the ZC method is complicated since either no zero crossing exists or the PBD-signal level at the zero-crossing point is so small that noise makes its accurate determination impossible [33-34].

This problem can be solved by applying the multiparameter fitting method proposed by Rantala et al.[34-35] or by using instead of air a medium with a diffusivity near to that of the sample.

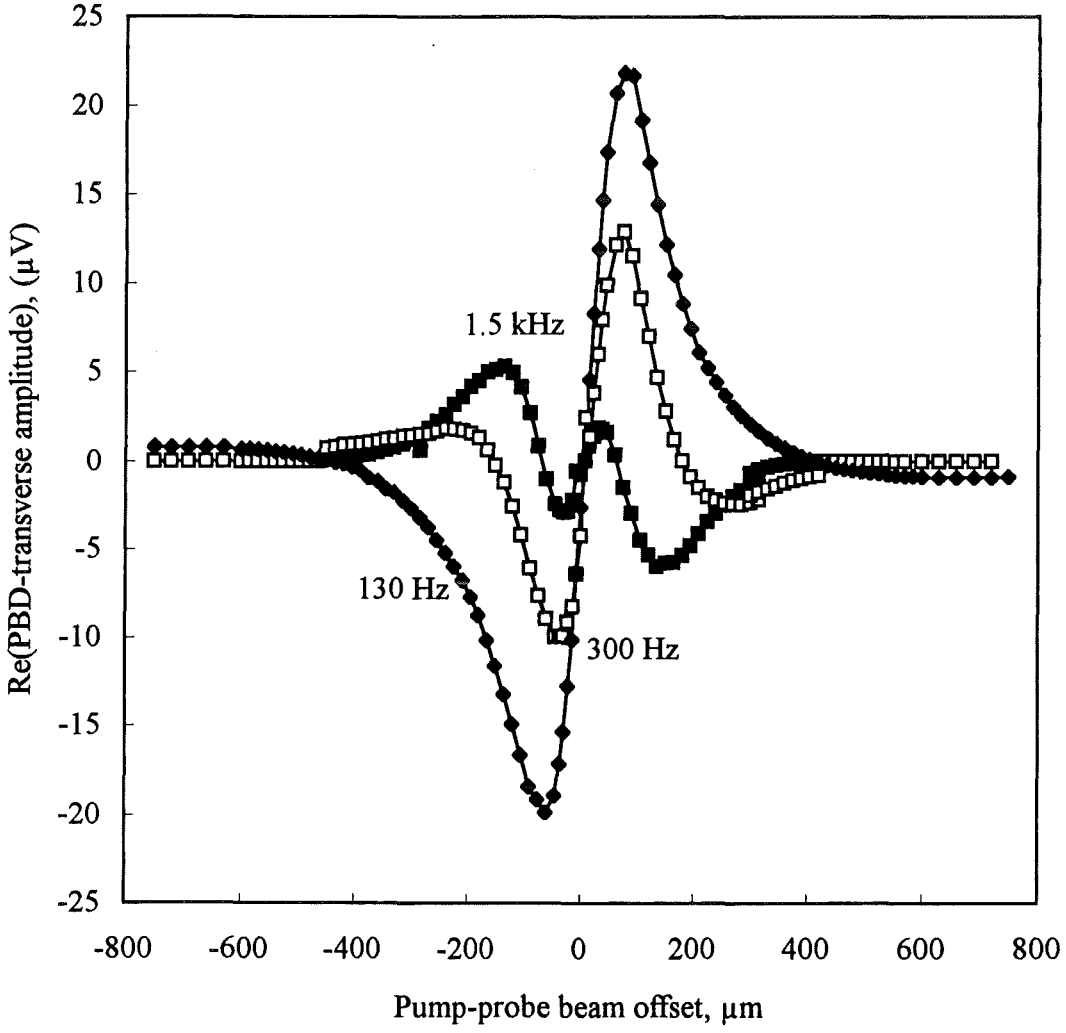

Fig.8 Real part of the experimental PBD-transverse amplitude versus pump-probe beam offset for the indoor side of the patinated sample #1 at different modulation frequencies.

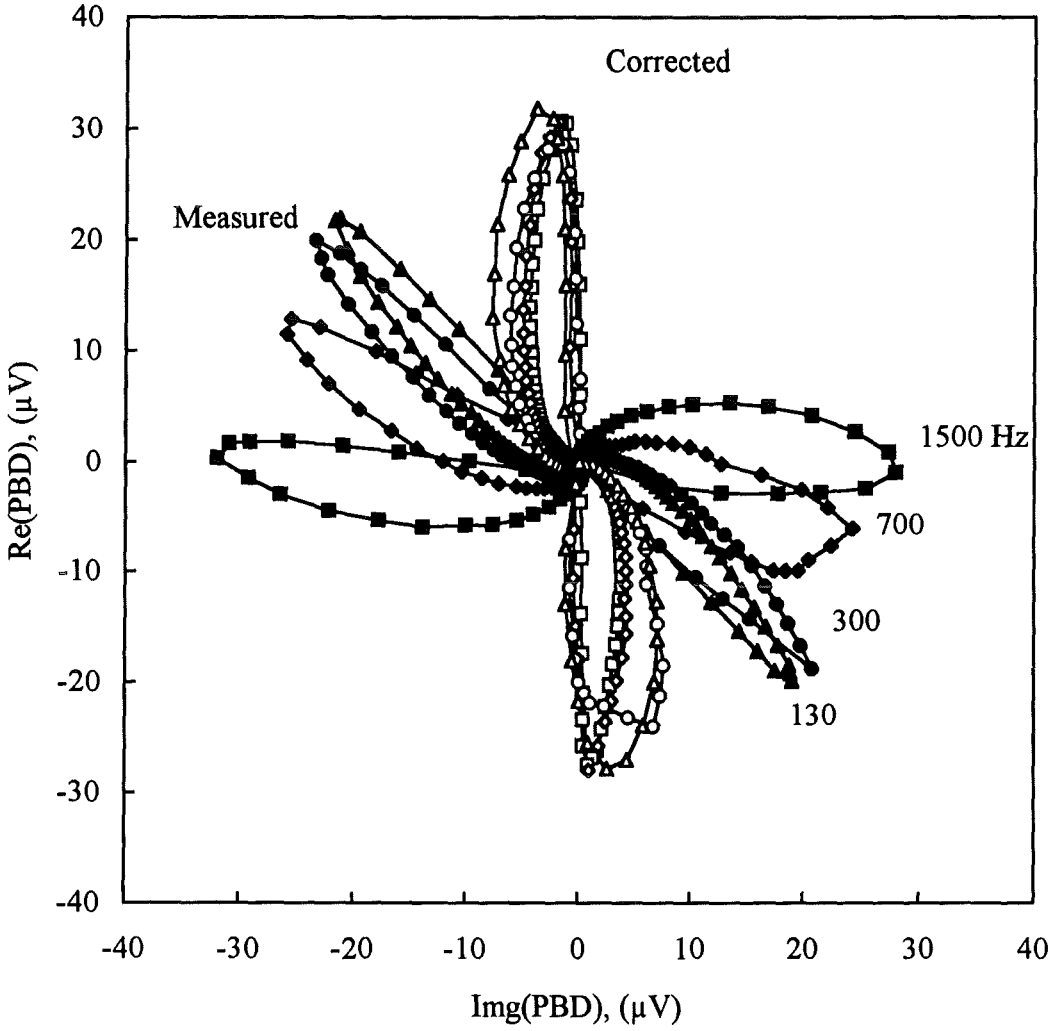

Fig.9 Argand diagrams for the indoor side of the patinated sample #1 at different modulation frequencies as measured in experiment and after correction (rotation in the complex plane of the loops axes which keeps them in a vertical position).

1.3.3 Results for the outdoor patina layer

In our case no zero crossings (like those shown in Fig.8) were observed in the measurements of the outdoor patina layer in air. To overcome this problem we used as a deflection medium liquid CCl_4 which has much lower thermal diffusivity ($\alpha = 8 \cdot 10^{-4}$ cm^2/s, [36]) than that of the air. It has been carried out by immersing the sample into a special optically transparent cell containing CCl_4.

The results of the zero crossing measurements of the outdoor and indoor patina layer are shown in Fig.10.

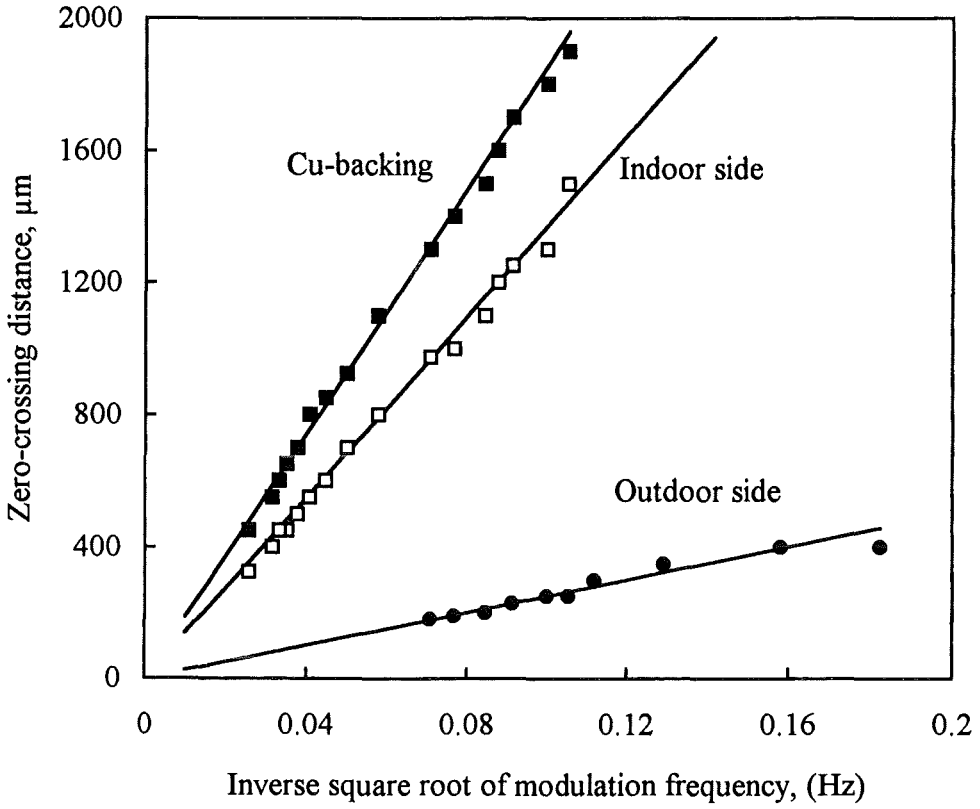

Fig.10 Measurements of the dependence of the zero-crossing distances on the inverse root of the modulation frequency for the outdoor and indoor sides of the patinated sample #1 and for clean Cu. The fitted slopes of the straight lines give the values of the thermal diffusivities.

A clean Cu sample (i.e. after removal of the outdoor patina layer) was used as a reference because the thermal diffusivity of copper is well known and has been also measured by the PBD method [30]. The fitted slopes of the straight lines give the values of the thermal diffusivities according to equation (5). For the calculations of α we used γ=1 which corresponds to opaque thermally thin materials [32].

For the reference Cu sample we obtained α_{Cu} = 1.1 cm^2/s which is in good agreement with literature data and the results of alternative measurements by means of the PBD method (α_{Cu} = (1.0-1.2) cm^2/s, [30]). A significant difference between measured thermal diffusivities of the outdoor and indoor patina layers is possibly due to the different morphology of these patinas.

The outdoor patina layer which has been exposed to the atmosphere has a poor thermal diffusivity α_{otd} = 0.022 cm^2/s which is very close to those of brochantite $Cu_4(OH)_6SO_4$ (0.025 cm^2/s) as calculated from the values of thermal conductivity (κ), heat capacity (c) and density (ρ) [37-39].

In contrast to the outdoor layer, the inner patina layer shows relatively high thermal diffusivity α_{ind} = 0.6 cm^2/s which is only by a factor of two lower than that of copper. This is probably due to the fact that this indoor layer has a quite nonuniform morphology and thickness which can be clearly seen in the photothermal images (see Chapter 3). Thus, measured value of α_{ind} can be much higher than the real one due to the influence of Cu backing material.

It should be also pointed out that the results of α_{otd} and α_{ind} measurements are mean values averaged over the sample surface area of about 1 mm^2 due to linear scanning of the probe beam. A more realistic value of α_{ind} = 0.02 cm^2/s corresponding to that of cuprite Cu_2O (which is the basic component of the initial patina growth process [10]) has been taken for the following analysis.

The accuracy of the thermal diffusivity measurements for the outdoor side of the patinated sample has been estimated to be about 10% which is a typical value for photothermal results [18,33].

1.3.4 Measurement of patina layer thickness

The possibility to vary the sampling depth in the PBD method has been used for a noncontact measurement of the outdoor and indoor patina layer thickness. It has been carried out by measuring the amplitude and phase of the normal Φ_n component of the PBD signal as a function of the pump beam modulation frequency.

Typical frequency dependencies of the PBD amplitude and phase measured on the outdoor side of sample #1 are shown in Figs. 11(a) and 11(b), respectively.

As it can be clearly seen from Figure 11(a) there are three frequency regions corresponding to the contributions of different layers of the sample to the total PBD signal.

Below the first characteristic frequency (f_1=80 Hz) the thermal diffusion length μ is higher than the total sample thickness (Fig. 11(c)). At f_1 μ is approximately equal to the Cu-backing thickness and above the second characteristic frequency (f_2=1600 Hz in this case) the thermal waves are completely inside the outdoor patina layer.

Thus, by varying the pump beam modulation frequency, one can follow the changes of the thermal waves due to different layers of the sample as it is depicted schematically in Fig. 11(c). The outdoor patina layer thickness l can be estimated from the simple relation (see eq.(4)):

$$l = (\alpha/\pi f_2)^{1/2} \tag{6}$$

where the thermal diffusivity α is supposed to be measured independently. Otherwise, the thermal diffusivity can be deduced by knowing l.

It should be noted that, regarding the differences in the PBD-amplitude (Fig. 11(a)) and phase (Fig. 11(b)) behaviour between corresponding frequency regions, the phase, being essentially the propagation time of the thermal waves through the material, shows more distinct frequency dependence. In addition, it is independent on the pump power and is, therefore, more suitable for further calculations.

The same procedure as described above was applied for the measurements of the indoor patina layer thickness.

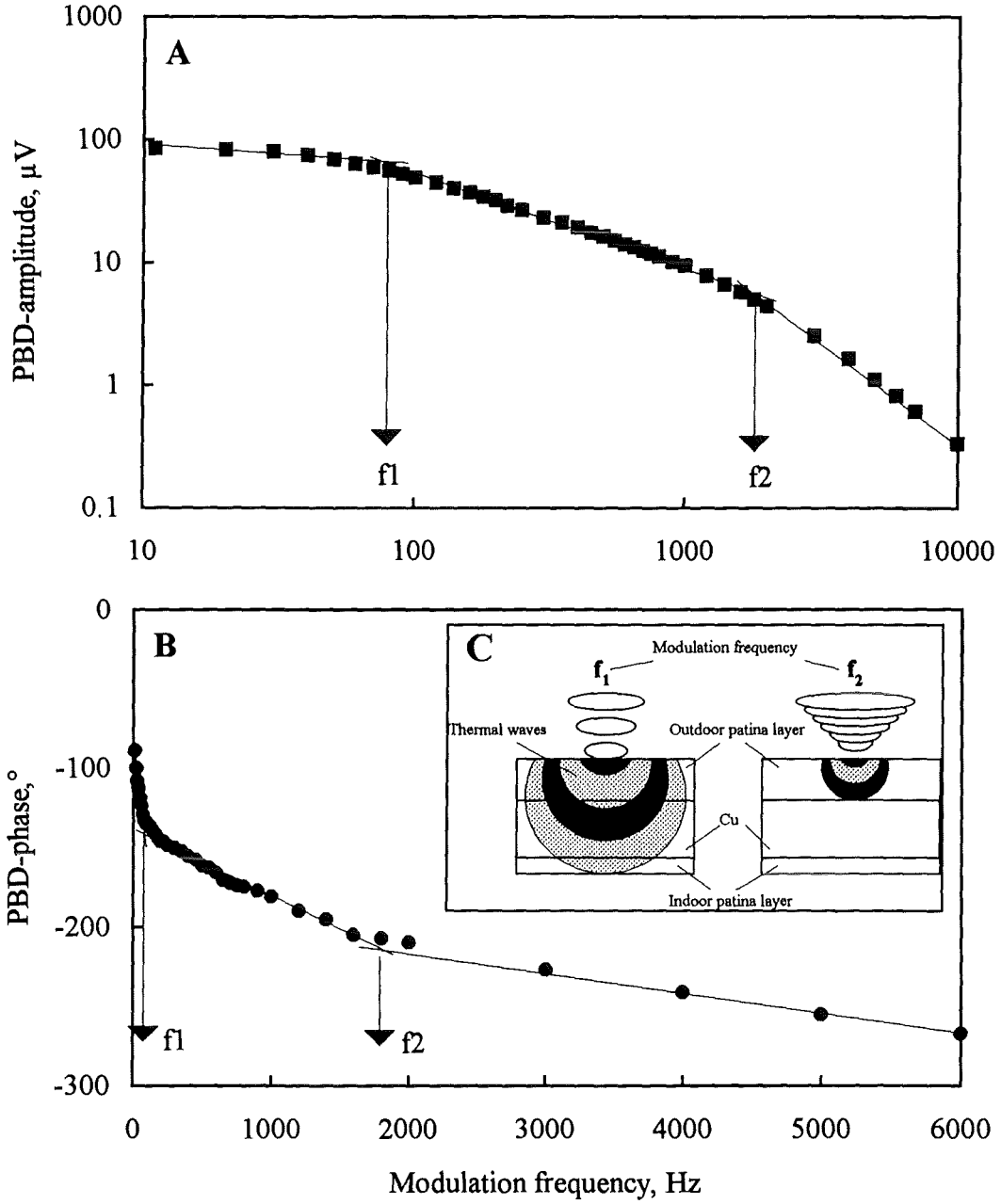

Fig.11 Frequency dependencies of the PBD-signal amplitude (a) and phase (b) measured on the outdoor side of the patinated sample #1 at 1064 nm and a schematic diagram of the thermal waves for two characteristic modulation frequencies (c).

Using the values of thermal diffusivity previously measured the mean outdoor and indoor patina layer thickness were calculated according to equation (6).

The value of l = 23 μm obtained for the outdoor patina layer is in reasonable agreement with that of the same material deduced from Auger electron spectroscopy depth profiles [13]. The corrosion rate has been evaluated to be ca. 0.4 μm/year for the outdoor layer which is typical values for the patinas [29]. For the indoor patina layer we found l = 10 μm.

The accuracy of the measurements of the characteristic frequencies has been estimated to be about 20%. No differences in characteristic frequencies were noted for different pump beam wavelengths.

Chapter 2
Photothermal Imaging of the Patina

2.1 Phase and Amplitude Imaging

In this Chapter several photothermal images are presented obtained from the outdoor and indoor patina layers.

One of the main advantages of photothermal imaging is its capability to separate on-surface (optical) and sub-surface features. The amplitude of the PBD-signal depends on both surface inhomogeneties such as varying absorption coefficients, surface morphologies and sub-surface features. The phase is independent on the difference in absorption and depends only on the sub-surface features provided the optical features are thermally thin, i.e. their characteristic thickness is much less than the thermal diffusion length [22, 40].

Another important advantage of monitoring the phase is its high penetration depth compared to amplitude. It has been shown theoretically and experimentally that phase imaging can probe twice as deep as amplitude imaging [41-42].

In the case of such a complex material as patina there are several parameters influacing the contrast of a photothermal image. Generally they can be divided into three categories:

- surface morphological features, i.e. surface roughness, porosity or inhomogeneties in patina layer thickness occurring during patina formation;
- surface absorption features, i.e. difference in optical absorption from point to point along the surface caused by the nonuniformities of patina structure and by the presence of incorporated particles;

- different kinds of sub-surface features such as cracks, domain boundaries, bulk includings, etc. All these circumstances have to be taken into account in the analysis of the photothermal images of patinated samples.

The spatial resolution in thermal wave microscopy is limited by either the pump beam spot size on the sample surface or the thermal diffusion length, whichever is larger. When the pump radiation is strongly focused, the spatial resolution increases with increasing modulation frequency.

2.2 Imaging Procedure

A photothermal image which is actually a map of the local temperature distribution on the sample surface is obtained by point-by-point raster scanning. In the present work scanning was performed by means of a step-by-step motion of the sample mounted on a X-Y translation stage with two step motors in either direction.

Both the PBD amplitude and phase of the normal Φ_n deflection of the probe beam have been processed by a lock-in amplifier and stored in a personal computer for further treatment. The computer software [43] allowed to obtain both 2-D and 3-D images in different colour representations as well as to perform layer-by-layer analysis of the images.

For the photothermal imaging of the patinated samples the pump beam was focused to 40 μm spot size (1/e) using a system of lenses (Fig.2). The modulation frequency used lies in the interval from 0.5 kHz to 5 kHz.

The thermal diffusion lengths in this frequency region vary from 40 μm to 12.6 μm for the outdoor patina layer. So, in the case of the outdoor patina layer the spatial resolution was defined only by the pump beam spot size and supposed to be constant for all measurements.

2.3 Photothermal Images of the Outdoor Patina Layer

2.3.1 Amplitude and phase images

The first series of the photothermal images were obtained from the outdoor patina layer of sample #1 using a He-Ne pump laser modulated at 500 Hz, 1 kHz, 3 kHz and 5 kHz. An optical image of the outdoor side of this sample obtained by using an optical microscope is presented in Fig.12.

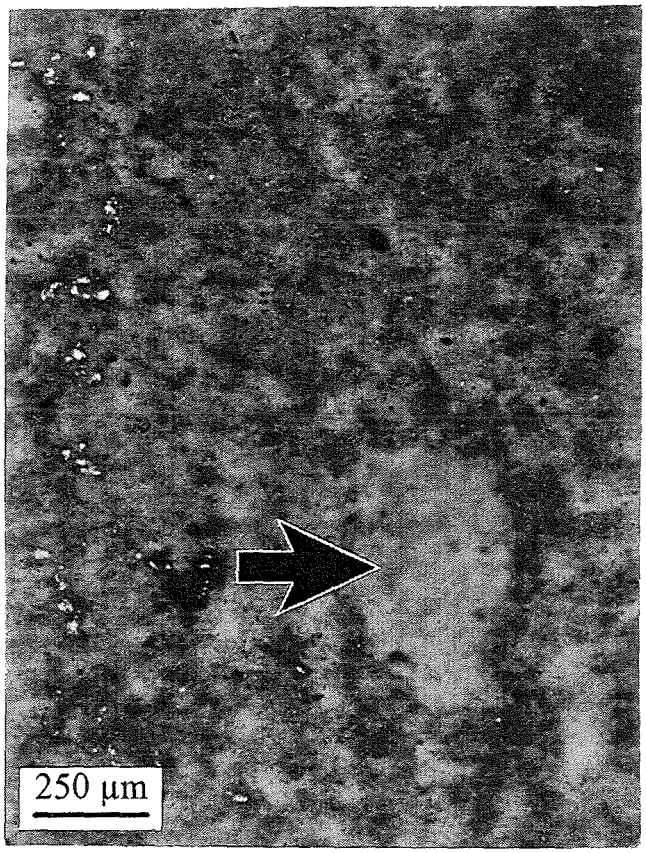

Fig.12 Optical image of the outdoor side of the patinated sample #1.
Black arrow show the position of the green spot, as discussed in the text.

Fig.13 serie shows the PBD amplitude (a-d) and phase (e-h) images obtained at 633 nm at different modulation frequencies.

We used a 15-colour representation for each image since in this case the contrast is more clear. The PBD-amplitude and phase scales are different (but they are the same for the whole group of images): from 0 to 450 arbitrary units for the amplitude images (i.e. 30 a.u./colour) and from 0 to 3000 units (200 a.u./colour) for the phase images.

As it can be clearly seen from these figures the outdoor patina layer is quite nonuniform and has a complex surface structure with a lot of different features. The main feature is the surface morphology, i.e. surface roughness and porosity, appearing in form of spots (yellow, green or red depending on the colour representation).

The surface morphology became clearer visible with increasing pump beam modulation frequency as can be seen from a comparison of Figs. 13(a) - 13(d) and Figs. 13(e) - 13(h). This is due to the fact that at 3 kHz modulation frequency the thermal diffusion length is less than the outdoor patina layer thickness, and only this layer contributes to both the PBD amplitude and phase total signals.

As mentioned previously, the PBD-phase is sensitive essentially to the sub-surface features and to surface roughness, thus the phase images at high modulation frequencies represent the patina layer surface morphology (Figs. 13(g) and 13(h)).

The outdoor patina layer morphology is not disordered and was found to be oriented along axes between 60° and 90° with respect to the horizontal direction (see, for example, Figs. 13(c)-13(d) and Figs. 13(g) - 13(h)). This feature is probably due to the orientation of the sample at the roof during exposure.

Note that the oriented structure of the patina layer can not be observed optically (Fig.12) and appears on the photothermal image due to the thermal nature of the PBD-signal mapping not only on-surface features but also the bulk structure.

Two types of characteristic features which were detected several times in the samples should also be discussed.

First there is a green spot of ca. 250x500 μm^2 dimensions marked by the black arrows in Figs. 12 and 13(a) - 13(h). It is a piece of incorporated external material (probably metal) covered by the patina layer. This spot has a thermal conductivity higher than the surrounding patina layer which results in a corresponding decrease of the PBD-amplitude.

The presence of such a feature in both amplitude and phase images shows that it is also a surface nonuniformity. The thermal structure of this feature is much more extended than its visible part as it can be concluded from the comparison of the optical image (Fig. 12) and one of the photothermal phase images (Fig. 13(f)).

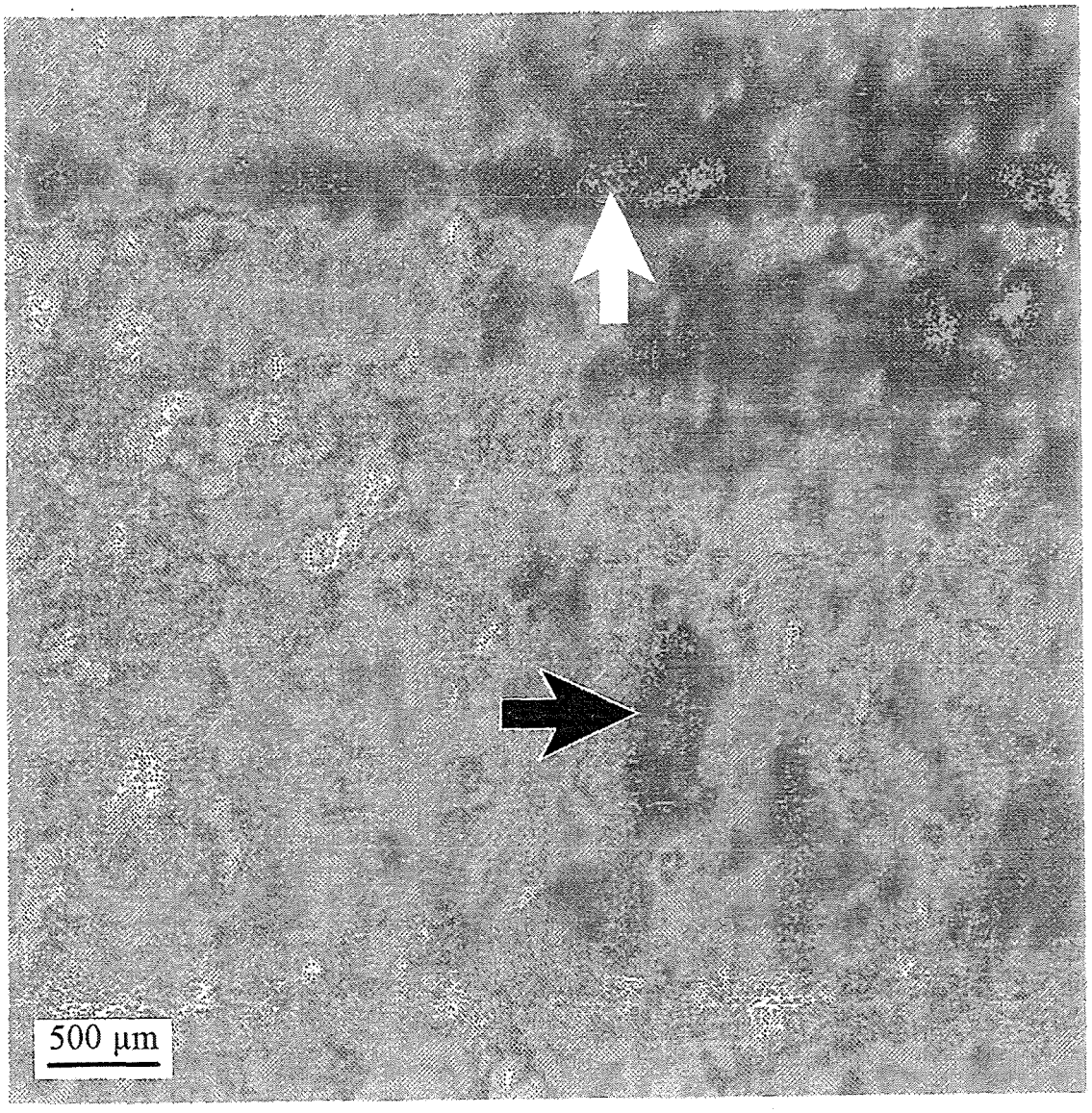

Fig.13a Photothermal PBD-amplitude image of the outdoor side of patinated sample #1 obtained at 0.5 kHz modulation frequency. Black and white arrows show the position of the green spot and the line band, respectively, as discussed in the text.

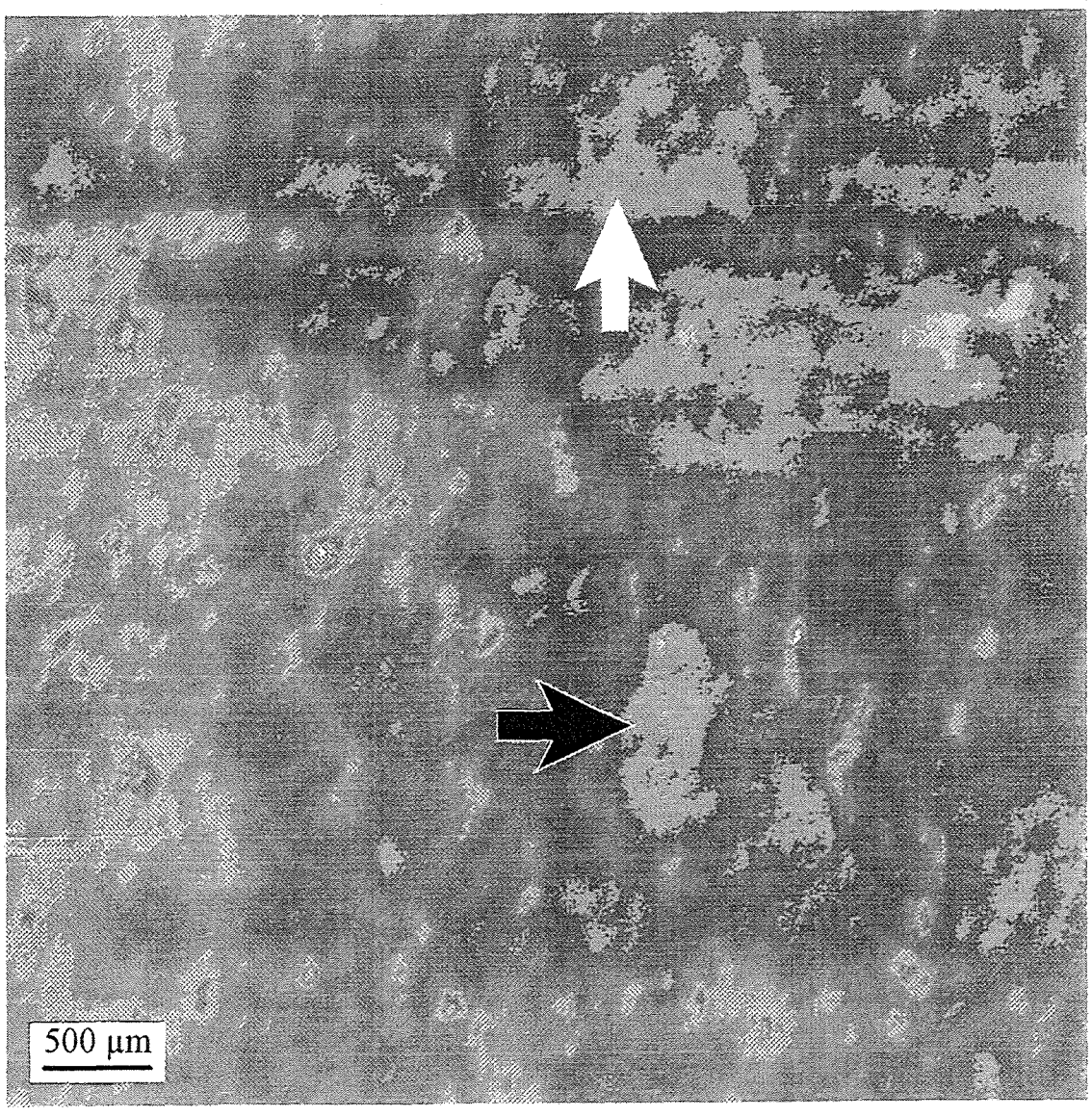

Fig. 13b Photothermal PBD-amplitude image of the outdoor side of patinated sample #1 obtained at 1 kHz modulation frequency. Black and white arrows show the position of the green spot and the line band, respectively, as discussed in the text.

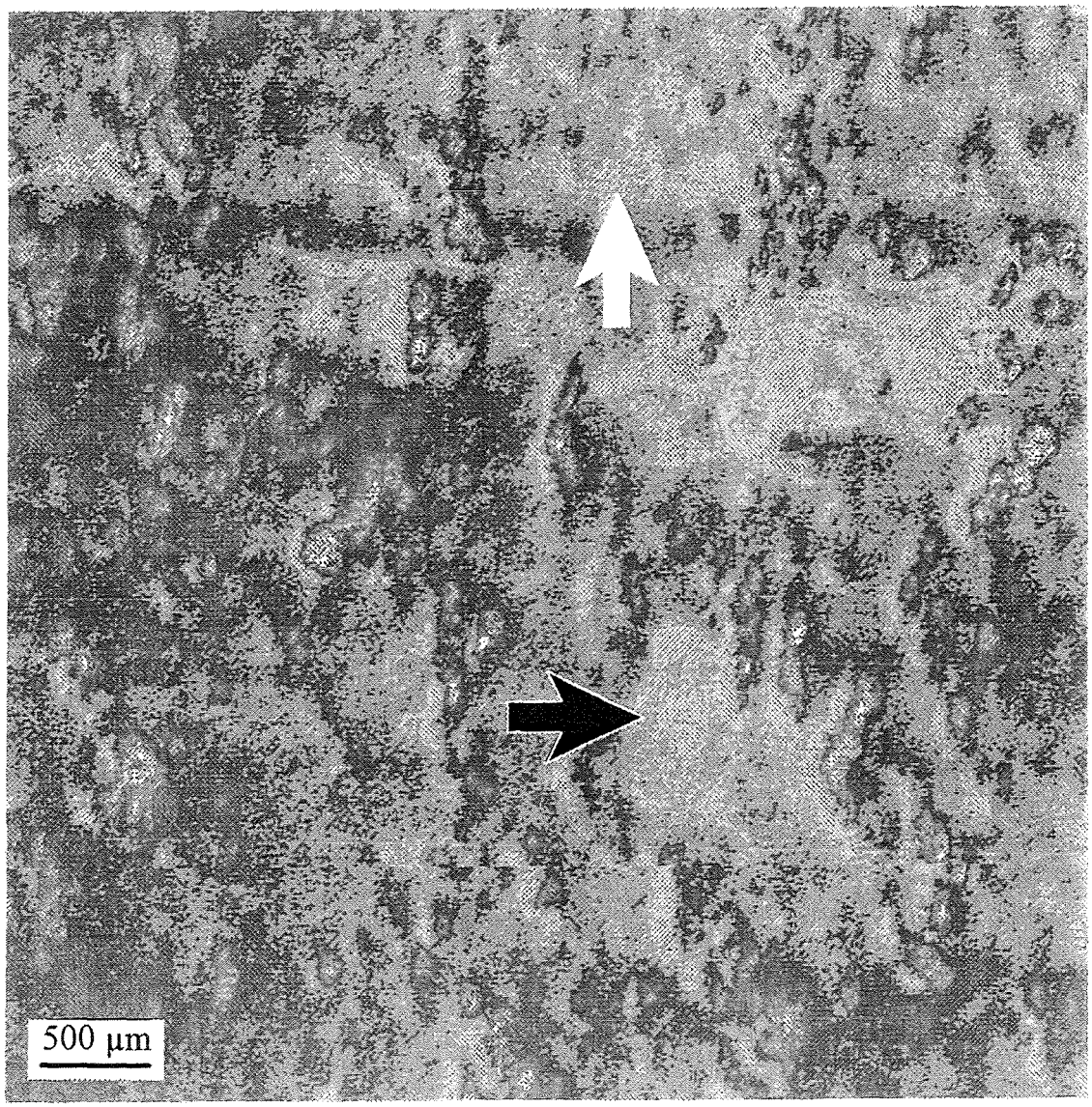

Fig.13c Photothermal PBD-amplitude image of the outdoor side of patinated sample #1 obtained at 3 kHz modulation frequency. Black and white arrows show the position of the green spot and the line band, respectively, as discussed in the text.

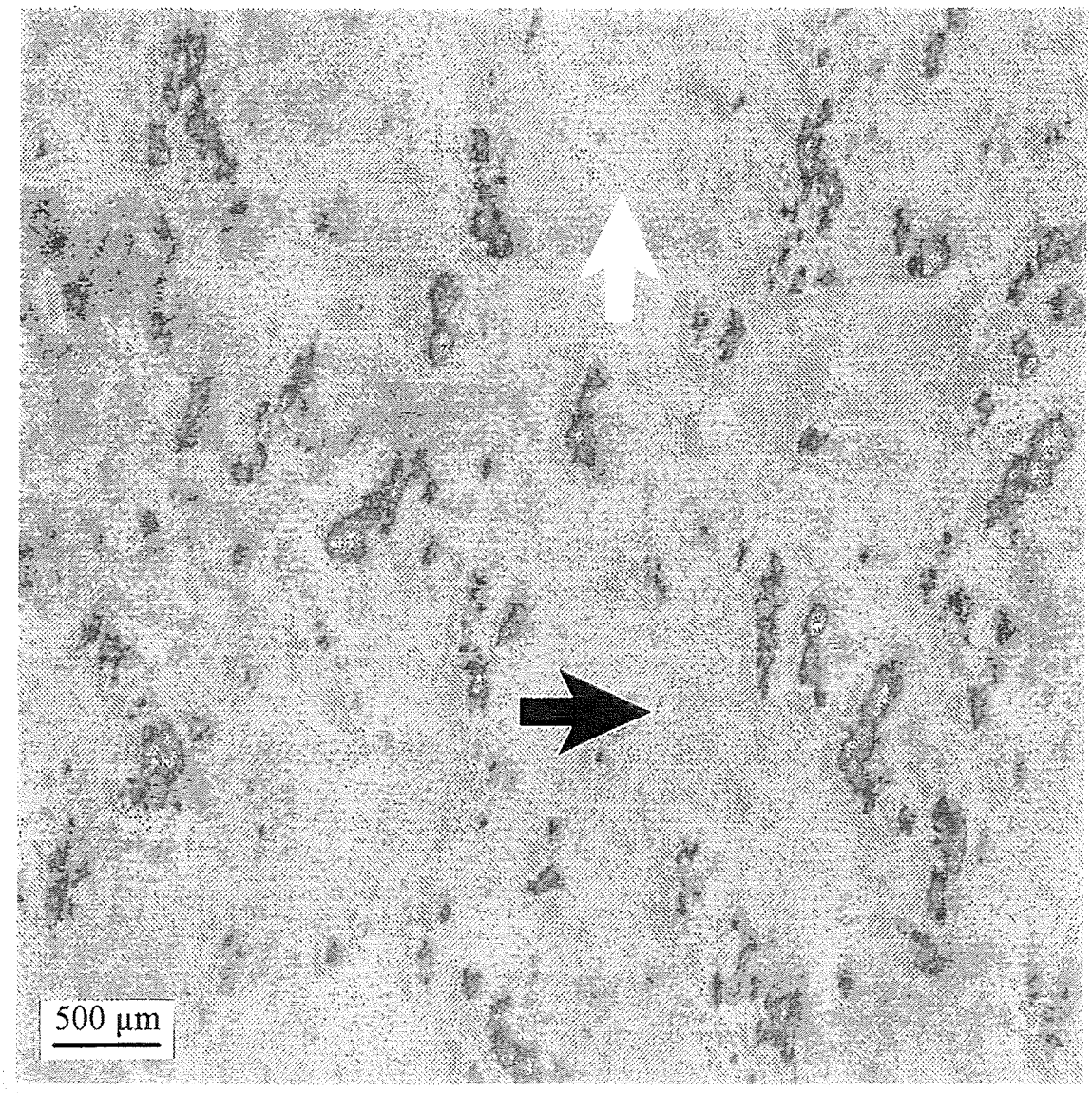

Fig. 13d Photothermal PBD-amplitude image of the outdoor side of patinated sample #1 obtained at 5 kHz modulation frequency. Black and white arrows show the position of the green spot and the line band, respectively, as discussed in the text.

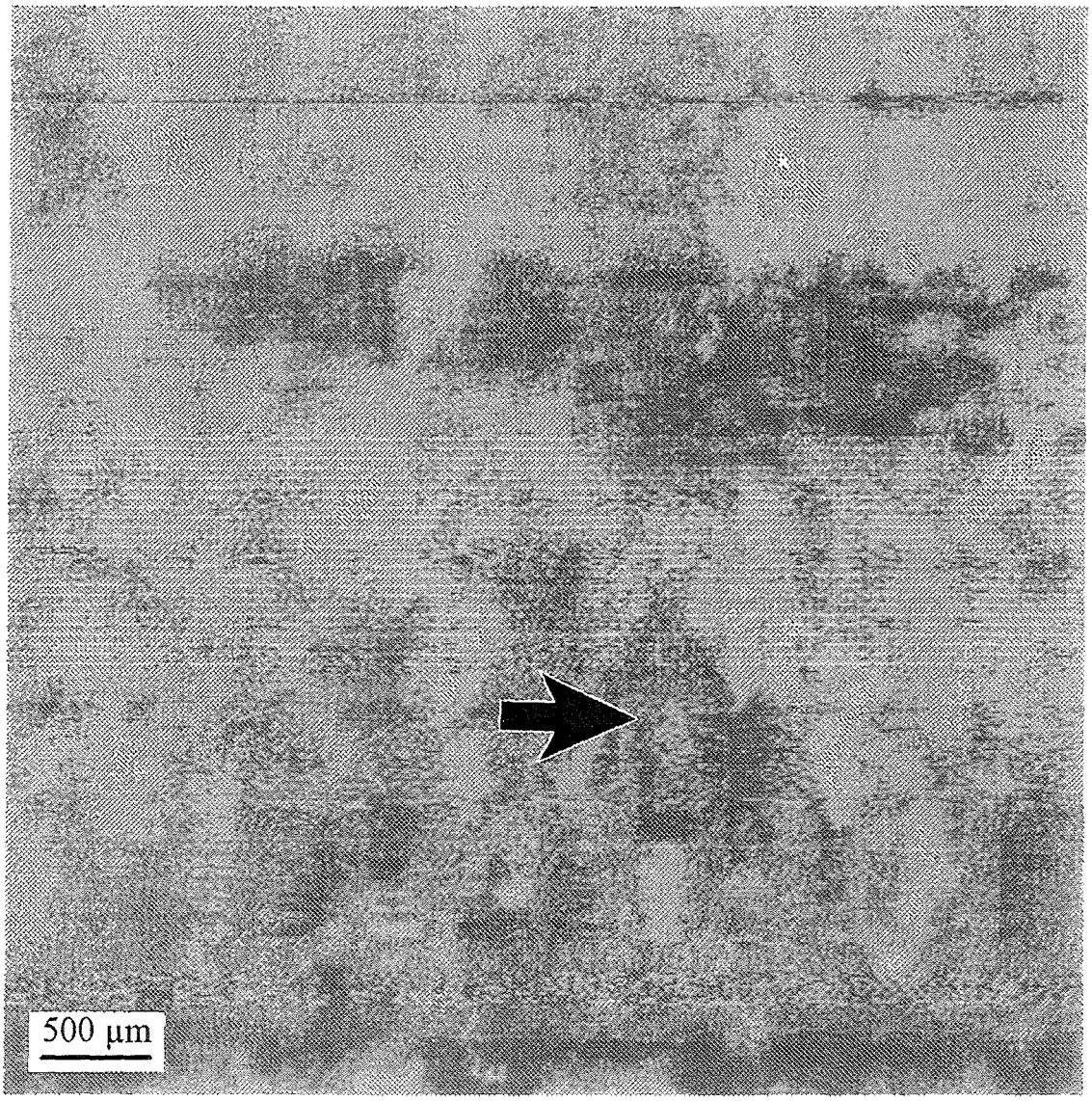

Fig.13e Photothermal PBD-phase image of the outdoor side of patinated sample #1 obtained at 0.5 kHz modulation frequency. Black arrow shows the position of the green spot, as discussed in the text.

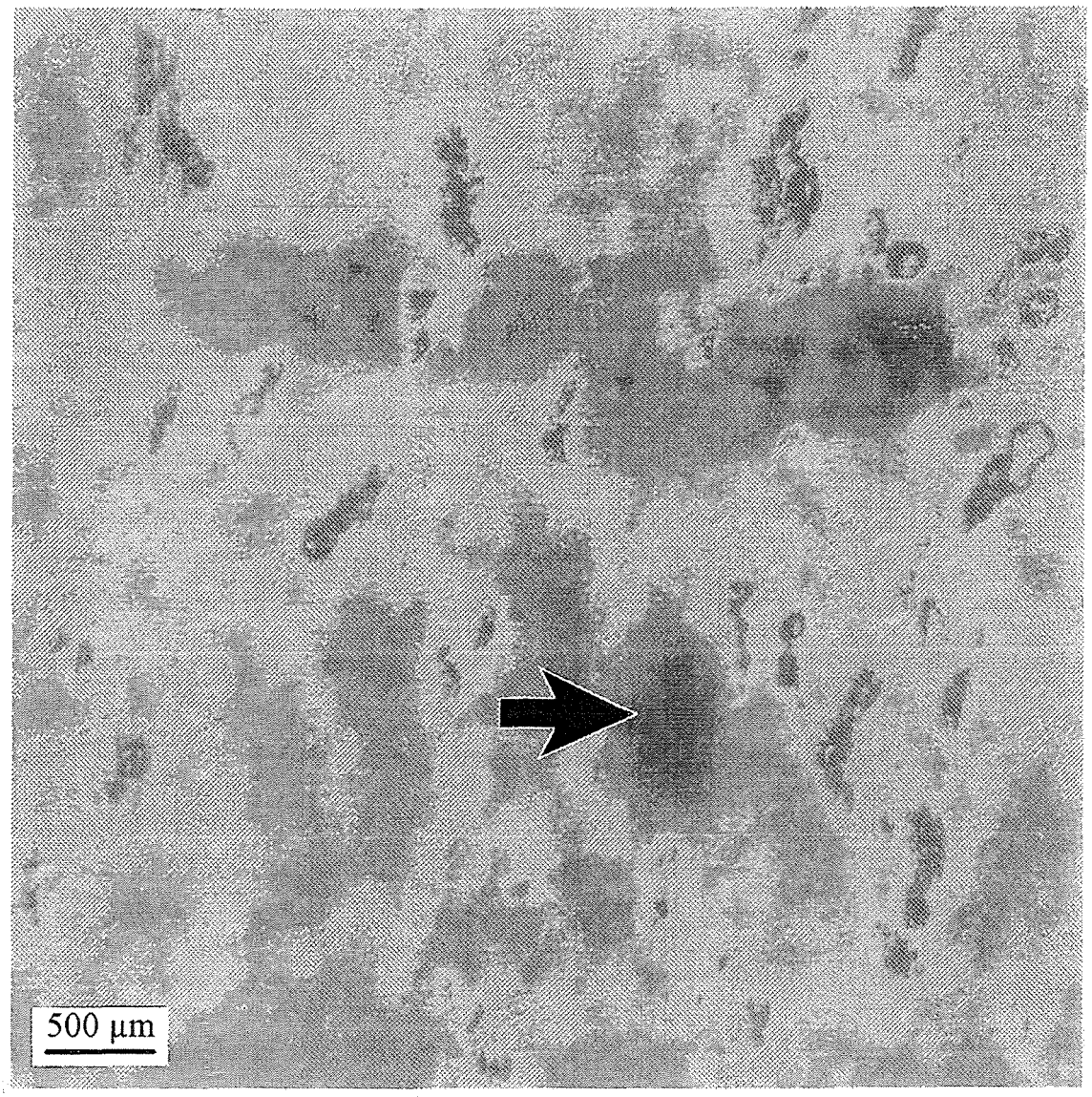

Fig.13f Photothermal PBD-phase image of the outdoor side of patinated sample #1 obtained at 1 kHz modulation frequency. Black arrow shows the position of the green spot, as discussed in the text.

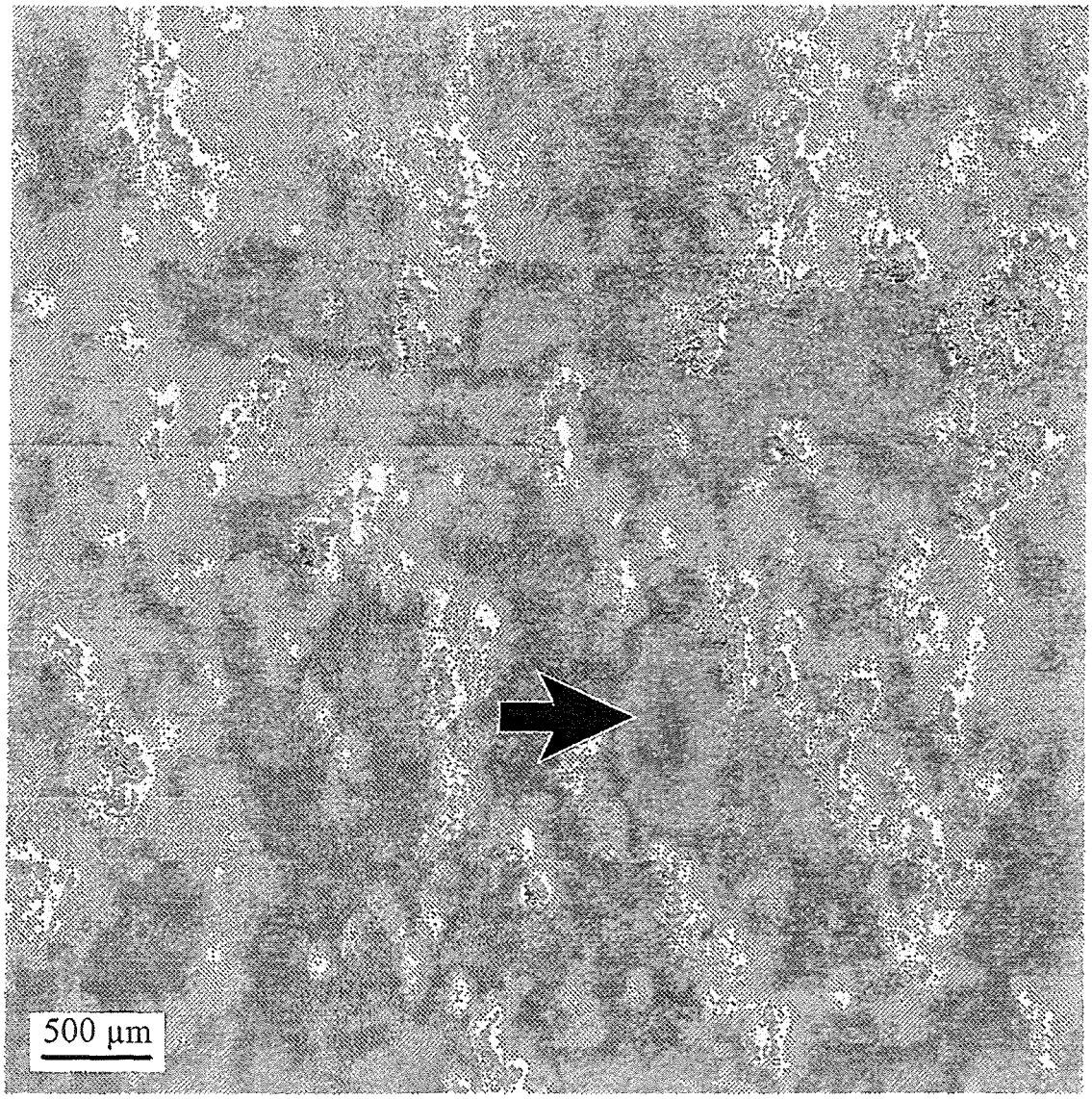

Fig.13g Photothermal PBD-phase image of the outdoor side of patinated sample #1 obtained at 3 kHz modulation frequency. Black arrow shows the position of the green spot, as discussed in the text.

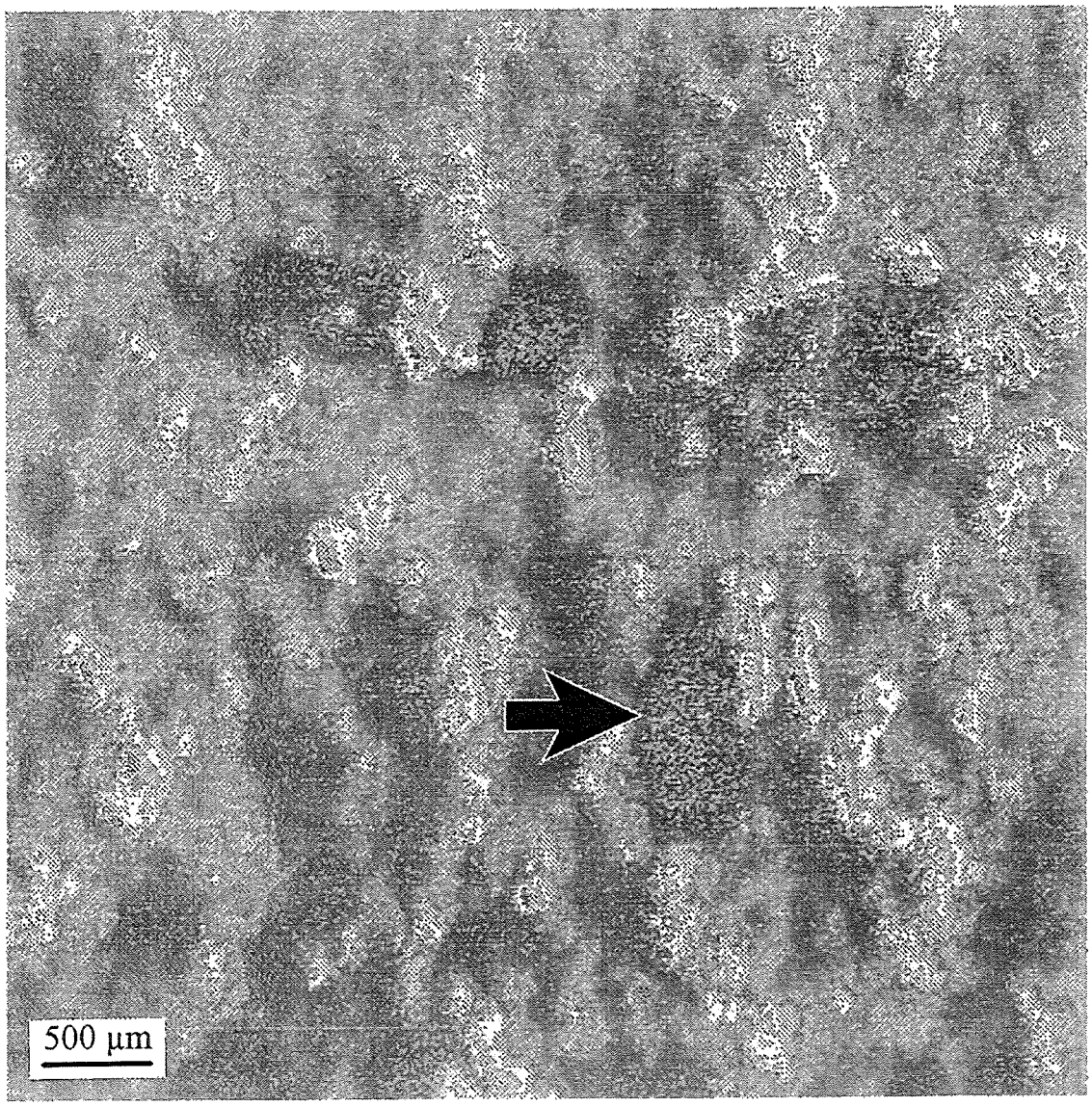

Fig.13h Photothermal PBD-phase image of the outdoor side of patinated sample #1 obtained at 5 kHz modulation frequency. Black arrow shows the position of the green spot, as discussed in the text.

It is also interesting to note that the internal thermal structure of this feature becomes more clear on the phase image with increasing modulation frequency and inversely, with decreasing frequency on the amplitude images. For example, at 5 kHz modulation frequency this feature is absent on the amplitude image (Fig. 13(d)) and quite clear on that of the phase (Fig. 13(h)).

Secondly, there is a horizontal band in the upper part of the amplitude images marked by the white arrows (Figs. 13(a) - 13(d)). It is a pure absorption feature on the sample surface without any sub-surface structure as this band is absent on the PBD phase images.

2.3.2 Influence of the pump beam wavelength

The influence of the pump beam wavelength on the photothermal image is illustrated in Figs. 14(a), 14(b) and 14(c).

It can be seen from these figures that changes in wavelength cause a variation of the optical absorption picture and that the oriented structure of the outdoor patina layer becomes clearer when the excitation wavelength is increased from 532 nm to 633 nm and further to 1024 nm.

Note, that the green spot discussed above is not uniform as it looks optically but has a fine structure.

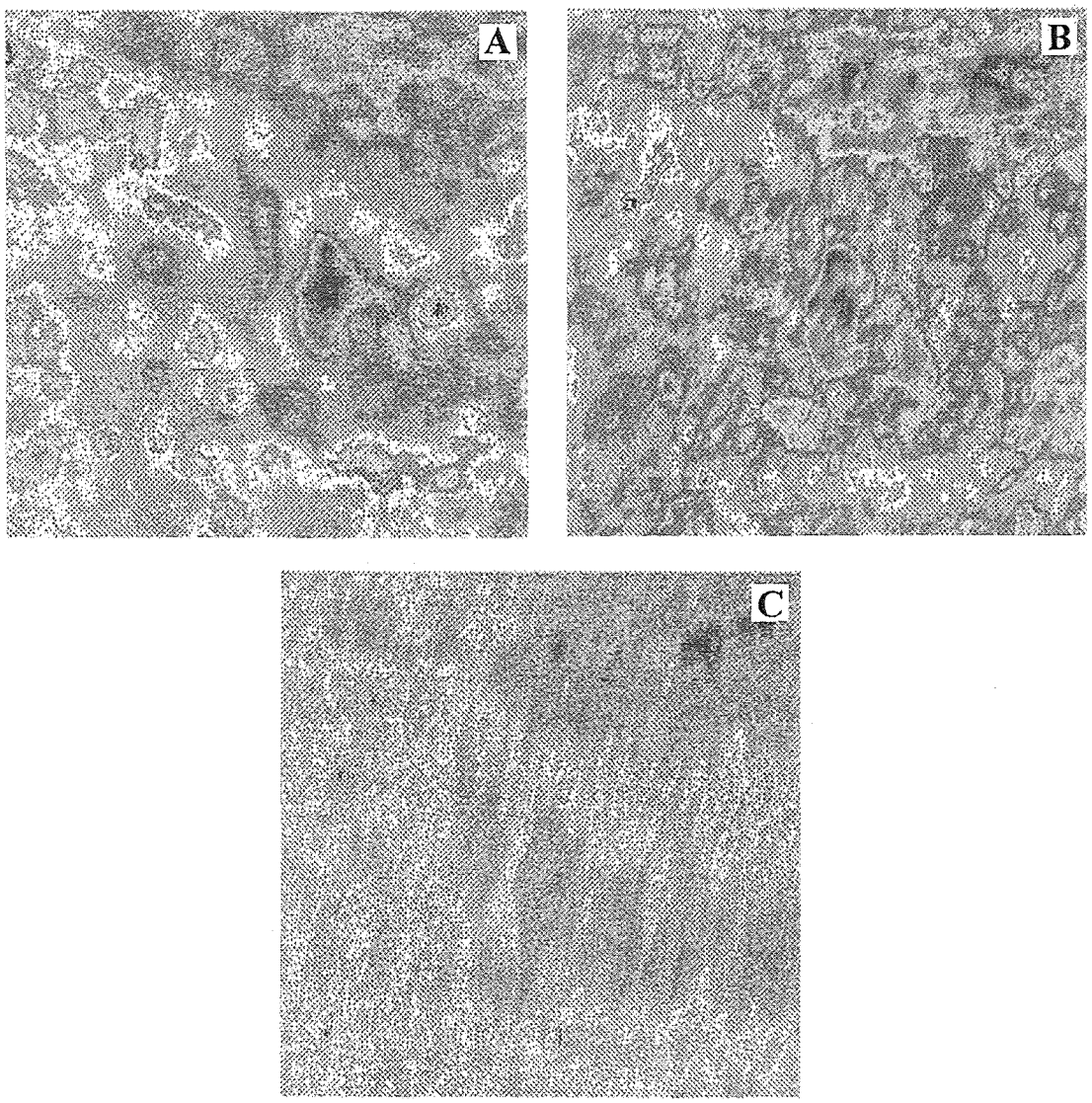

Fig. 14 Photothermal amplitude images of the outdoor side of the patinated sample #1 at 1 kHz modulation frequency obtained for different wavelengths of the pump beam: 532 nm (a), 633 nm (b) and 1024 nm (c).

2.4 Photothermal Images of the Indoor Patina Layer

The photothermal images of the indoor patina layer were obtained by using a Nd:YAG laser (1064 nm) as in the visible region this layer has a very low optical absorption. Typical photothermal images of the indoor side are presented in Figs. 15(a) and 15(b).

These images are quite different from those of the outdoor patina layer and show a great number of small includings of 50 - 100 μm in diameter. These features are probably the centres of the patina formation at an earlier stage of this process[10]. No oriented structure like that on the outdoor patina layer was observed.

Note that a spatial resolution evaluated from the image contrast in Figs 15(a) and 15(b) is better than the thermal diffusion length (μ=138 μm for 1 kHz modulation frequency). This is due to the local decrease of α compared to its mean value and corresponding increase in spatial resolution, so that these centers become visible.

The analysis of the PBD amplitude and phase images similar to that discussed previously shows the presence of a relatively large sub-surface feature marked by the arrows in the upper parts of Figs. 15(a) and 15(b).

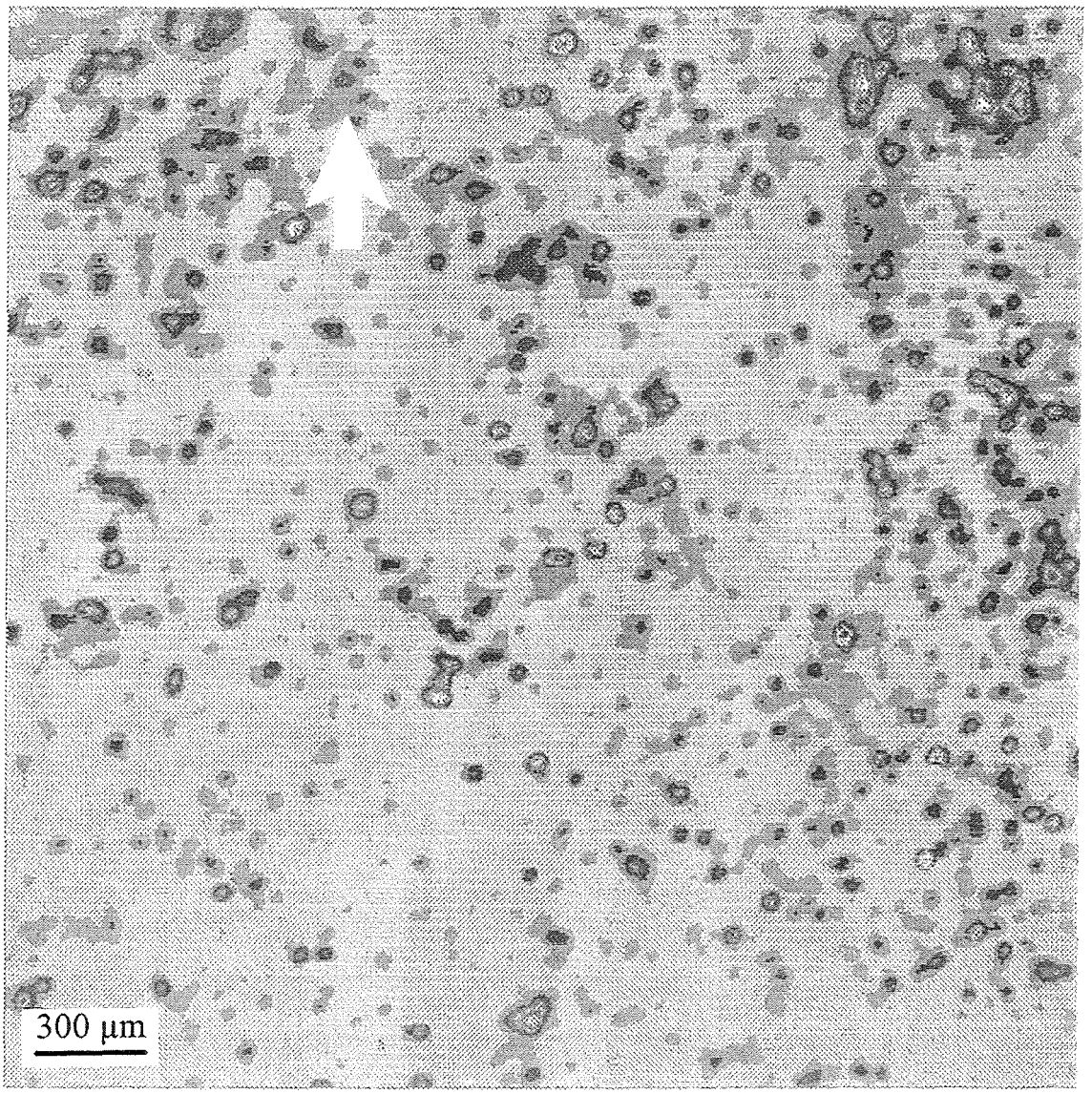

Fig.15a Photothermal amplitude image of the indoor side of the patinated sample #1 at 1 kHz modulation frequency and 1064 nm. Arrow shows the position of sub-surface feature, as discussed in the text.

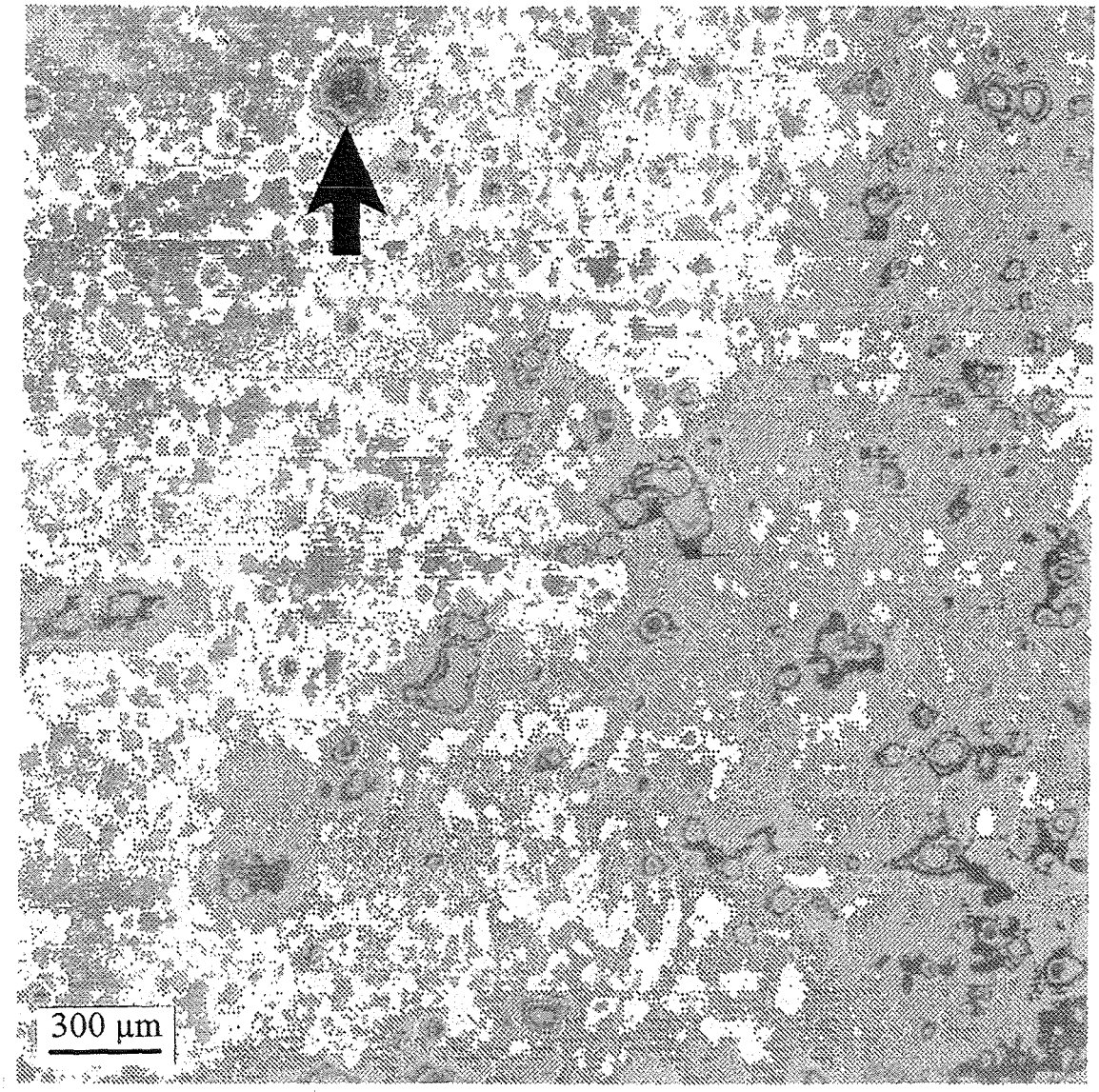

Fig.15b Photothermal phase image of the indoor side of the patinated sample #1 at 1 kHz modulation frequency and 1064 nm. Arrow shows the position of sub-surface feature, as discussed in the text.

2.5 Photothermal Images of the Black Spot On the Outdoor Patina Layer

As it has been mentioned earlier sculptures, roofs, and other objects made of copper or copper alloys and exposed to the atmosphere often have small black spots on their surface [4,29]. The structure of these spots is not well established as no systematic studies have been performed [4]. We have chosen such a spot on the outdoor patina surface for a photothermal analysis.

An optical image of this black spot of ca. 450x700 μm^2 is shown in Fig. 16. It looks like a piece of external material incorporated into the outdoor patina layer.

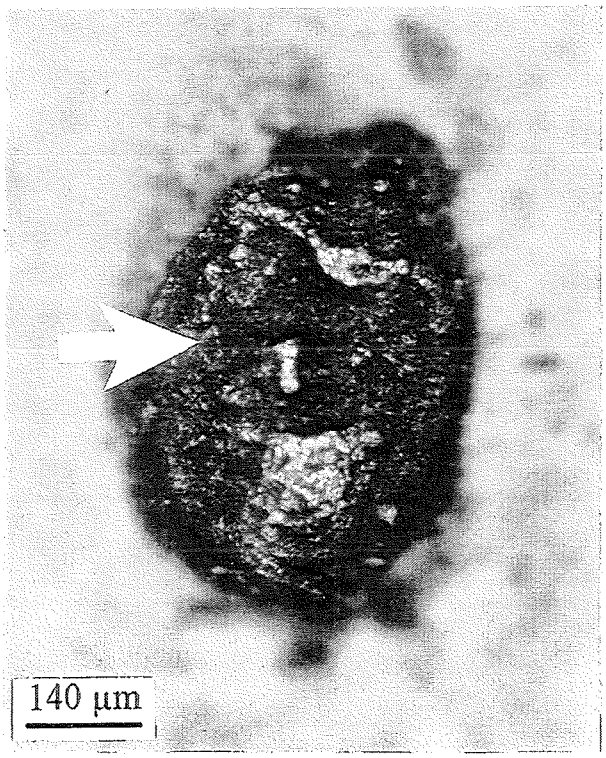

Fig.16 An optical image of the inclusion (black spot) on the outdoor patina layer of the patinated sample #2.

The corresponding PBD amplitude and phase images (Figs. 17(a) and 17(b)) show sharp boundaries without noticeable spreading of the thermal structure compared to its visible shape.

The phase image is nearly uniform along the surface of this spot except of one point (marked by the white arrow). The same point is observed in the PBD amplitude image where the signal is much higher than the mean value around. It is due to the presence of a small (ca. 50 μm in diameter) grain of different material which has much lower thermal diffusivity. Note that this feature is optically not clearly visible.

Another interesting feature is the difference in spot shape (in the upper part) between optical and photothermal images. The upper left branch of the spot marked by the black arrow in Fig. 17(a) is a part of the spot body covered by the patina layer. This branch is not seen in the optical view and appears both in the PBD amplitude and phase images. This fact allows us to conclude that the black spot was adhered to the surface prior to formation of the green patina layer.

Brief Summary to Chapters 1 and 2

In Chapters 1 and 2 we have presented the results of the first study in the framework of a new photothermal approach in patinated copper analysis.

It has been shown that the application of the relatively new nondestructive and noncontact photothermal beam deflection (PBD) method allows to obtain important quantitative information about the thermal properties of the patina as well as to perform measurements of patina layer thicknesses.

Photothermal imaging by using both the PBD amplitude and phase signals permits to study the thermal structure of the patina including the unique possibility to detect its sub-surface features like incorporated particles, black spots, etc.

It is assumed that the proposed photothermal approach can be a valuable technique complementary to other methods of patina analysis. The PBD method used in the present work is not the only suitable one among different photothermal detection schemes. An application of the PAS to the quantitative analysis of the main patina components from a spectroscopic point of view is presented in the following Chapter 3.

Based on the results obtained we propose in Appendix the principles of a new portable PBD-device for in-field measurements. This simple instrument could be used in different branches of modern *in-situ* environmental studies.

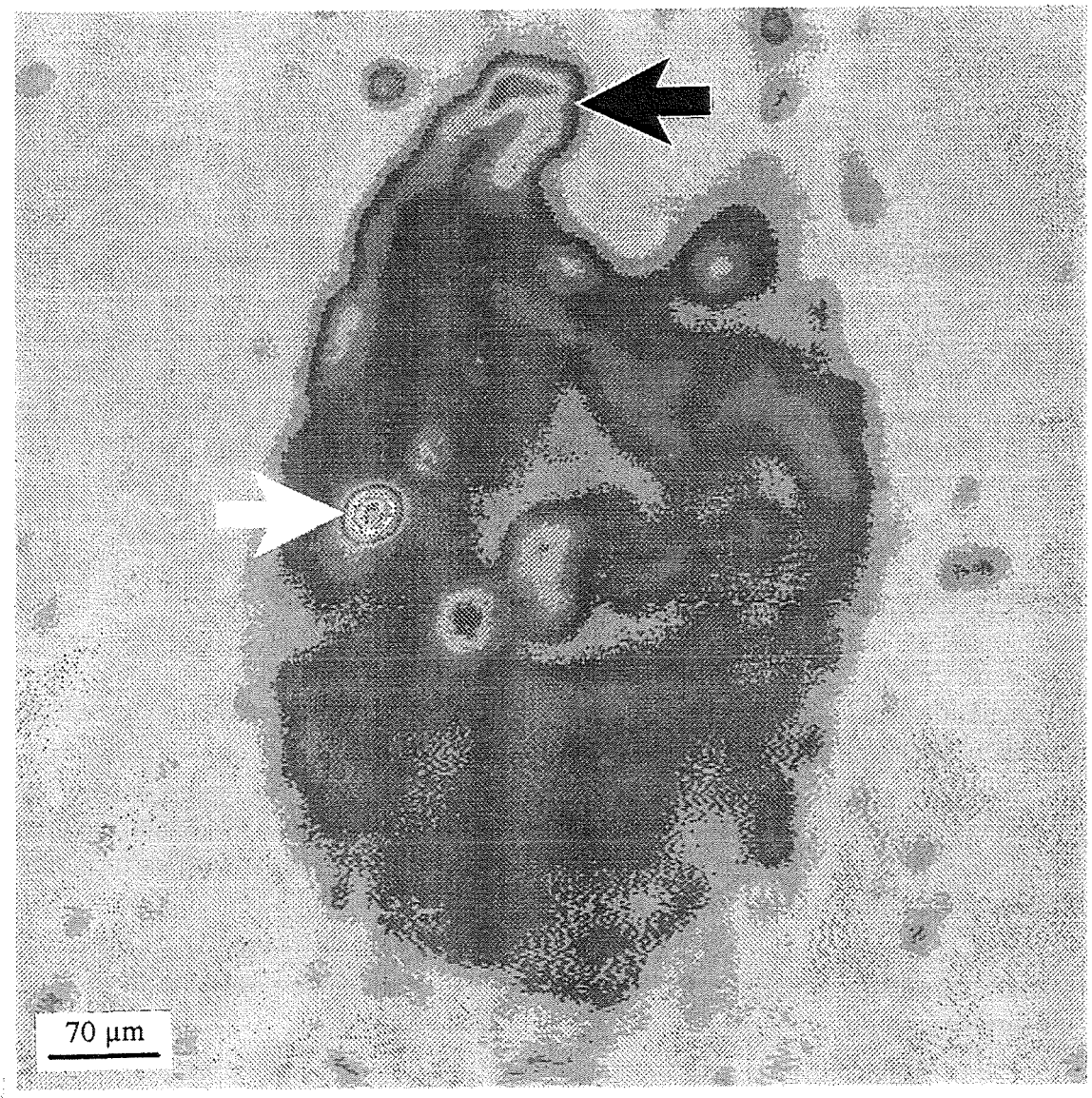

Fig. 17a Photothermal amplitude image of the inclusion (black spot) on the outdoor side of the patinated sample #2 obtained at 1 kHz modulation frequency and 1064 nm. White and black arrow show the position of the external material and the optically invisible part of the spot, respectively.

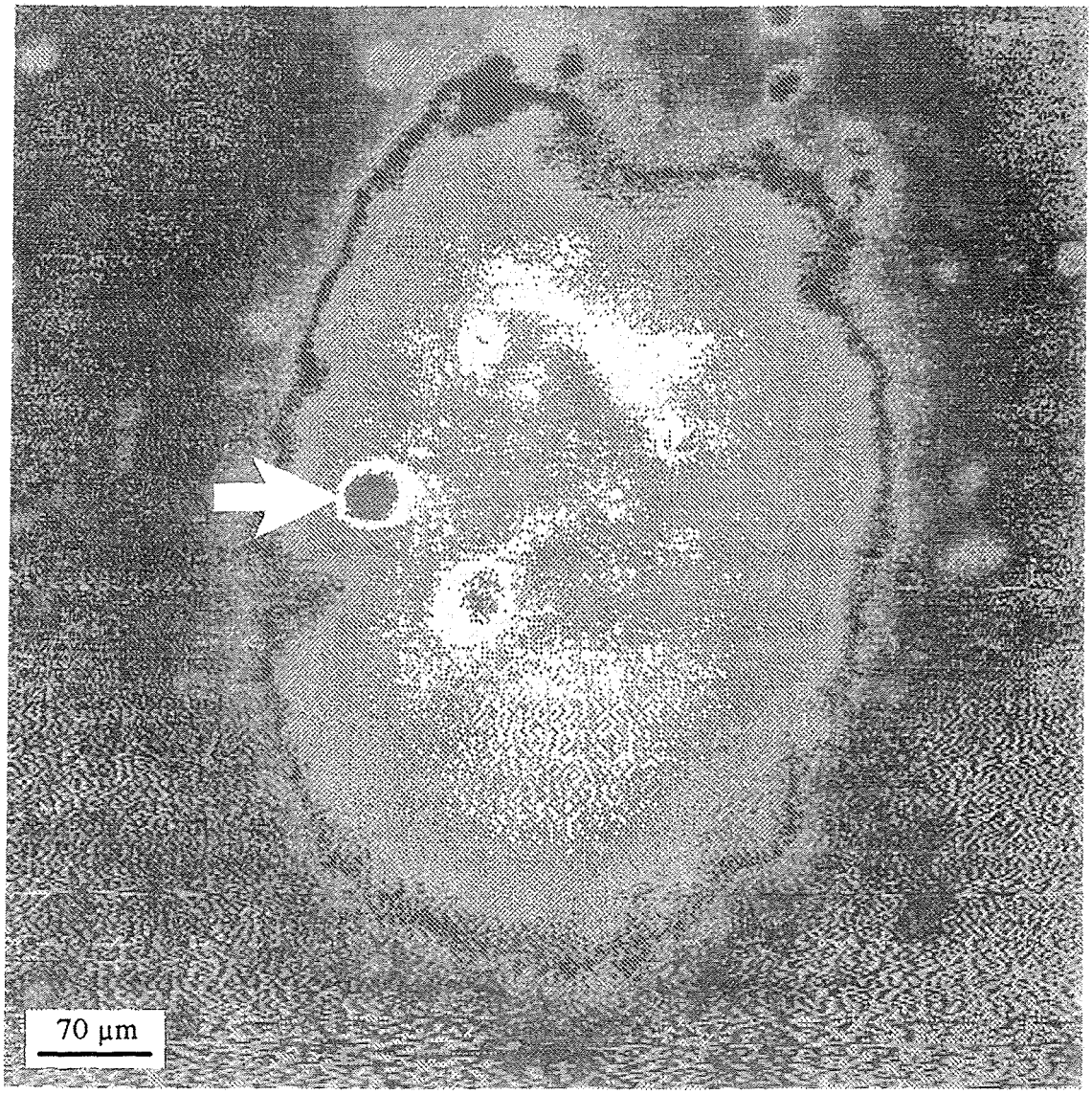

Fig. 17b Photothermal phase image of the inclusion (black spot) on the outdoor side of the patinated sample #2 obtained at 1 kHz modulation frequency and 1064 nm. White arrow shows the position of the external material, as discussed in the text.

Chapter 3
Photoacoustic FT-IR Spectroscopy of the Patina

Introduction

The opaque and highly scattering nature of the patina layers makes them difficult to study by traditional transmission- or reflection-based FT-IR spectroscopy. Infrared studies of patina require extensive sample preparation, which disrupts the morphology of the patina.

Poor reproducibility and sensitivity, combined with the limitation of conventional infrared spectroscopic techniques in providing only specific information on either the surface or the bulk regions of the sample, have led us to apply nondestructive and more sensitive FT-IR PAS to analysis of the patina.

Since the late 1970s, the use of photoacoustic spectroscopy has increased significantly, and, with the high throughput and multiplexing advantages of modern FT-IR spectrometers, FT-IR PAS can now be used as a routine analytical tool with good signal-to-noise ratio and without special sample preparation [44].

Briefly, the photoacoustic signal is generated when intensity-modulated infrared radiation absorbed by the sample converts into heat within the optical absorption depth. This heat diffuses to the sample surface and into an adjacent gas atmosphere. The thermal expansion of this gas produces the pressure change which is then detected by a microphone as the photoacoustic signal.

As only the photoacoustic signals generated within the thermal diffusion length are detected, this method can be used to discriminate between the surface and underlying layers of solid materials. A more detailed discussion of the PAS theory and thermal diffusion length is presented elsewere [45].

In the present Chapter, we report the use of FT-IR PAS to investigate the chemical composition of patinated copper samples, with particular reference to the depth distribution of the main patina components.

3.1 FT-IR PAS Experimental Set Up

All spectra were acquired on a Bruker IFS-66 (Bruker GmbH, Karlsruhe, Germany) spectrometer. Optical Path Difference (OPD) velocities in the range of 0.101 cm/s to 1.27 cm/s were used. These OPD velocities correspond to modulation frequencies from 404 Hz to 5080 Hz at 4000 cm^{-1} and from 40.4 to 508 Hz at 400 cm^{-1}.

An MTEC Photoacoustics (Ames, IA) Model 200 photoacoustic cell was used in all studies. Schematic view of this cell is presented in Fig. 18. The design of the MTEC 200 detector allows changing of the sample without removal of the sample cell from the spectrometer. In order to decrease the intensity of water-vapor bands and to increase the PAS signal, we purged the cell with dry helium for 10 min.

Two different sets of spectra were obtained, the first at 8 cm^{-1} resolution and averaged over 256 scans, and the second at 4 cm^{-1} resolution and averaged over 1024 scans. A MTEC carbon black reference sample was used as the reference material for all the spectra acquired. The same samples described in Chapters 1 and 2 were used.

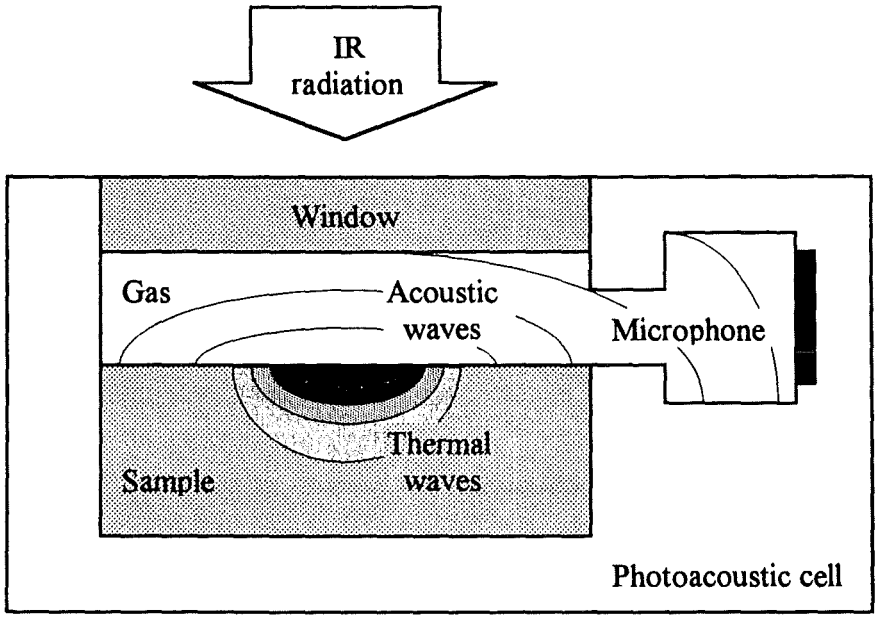

Fig. 18 Schematic view of the photoacoustic cell.

3.2 Photoacoustic Characterisation of the Samples

The photoacoustic signal depends on thermal, optical and geometrical parameters of the sample, and therefore different spectroscopic information can be obtained in relation to the values of these parameters [45].

3.2.1 Thermal diffusion length in the patina layer

The thermal diffusion lengths (μ) of patinated samples were calculated according to the Rosencwaig-Gersho (RG) theory for the photoacoustic effect in solids [45]. This parameter is given by the average thickness from the sample surface, which contributes to the PA signal (see equation (4) in Chapter 1) :

$$\mu = (2\alpha/\omega)^{1/2} \tag{6}$$

where ω is the angular modulation frequency which can be calculated from the modulation frequency, f :

$$\omega = 2\pi f, \; f = \upsilon\nu \tag{7}$$

where υ is the optical path difference (OPD) velocity of the interferometer and ν is the wavenumber of the IR radiation. In the Michelson design interferometer used in these experiments, ν is twice the value of the mirror velocity.

According to the RG theory, the thermal diffusion length is inversly proportional to the square root of the modulation frequency; therefore low optical velocities will result in PA signals from deep within the patina layer, while high OPD velocities will allow thermal diffusion from the surface region. This pattern is the basic for depth profiling analysis using FT-IR PAS.

The thermal diffusion lengths calculated according to (6) for the outdoor side of patinated samples are presented in Table I.

From these results it can be seen that μ decreases with increasing OPD velocity and wavenumber of IR radiation. Consequently, a high OPD velocity (at least 0.253 cm/s) is required in order to achive the thermal diffusion length comparable with the patina layer thickness (see also next section).

TABLE 1

Thermal diffusion lengths (in μm) for the outdoor side[a] of patinated sample as a function of the optical path difference (OPD) velocity of the interferometer.

Wavenumber	OPD velocity, cm/s						
cm^{-1}	0.101	0.139	0.190	0.253	0.316	0.475	0.633
4000	39.7	33.8	28.9	25.1	22.4	18.3	15.9
3500	42.4	36.2	30.9	26.8	24.0	19.6	16.9
3000	45.8	39.1	33.4	29.0	25.9	21.1	18.3
2500	50.2	42.8	36.6	31.7	28.4	23.2	20.1
2000	56.1	47.9	40.9	35.5	31.7	25.9	22.4
1500	64.8	55.3	47.3	41.0	36.6	29.9	25.9
1000	79.4	67.7	57.9	50.2	44.9	36.6	31.7
500	112.3	95.7	81.9	70.9	63.5	51.8	44.8
400	125.5	107.0	91.5	79.3	71.0	57.9	50.1

[a] Calculated with the use of the thermal diffusivity $\alpha_{otd} = 0.022\ cm^2/s$

The geometrical parameter is given by the thickness of the sample, i.e. the thickness of the outdoor or indoor patina layer (ℓ_{otd} or ℓ_{ind}) and the backing Cu substrate (ℓ_b = 600 μm).

The ℓ_{otd} and ℓ_{ind} values of the sample under study have been measured earlier by using the PBD method (Chapter 1). Obtained mean value ℓ_{otd} = 25 μm was in reasonable agreement with that of the same material deduced from Auger electron spectroscopy depth profiles [13]. The thickness of the indoor patina layer has been evaluated to be ℓ_{ind} = 10 μm.

3.2.2 Optical absorption length

The optical absorption coefficient (β) depends on the wavenumber of the radiation, thus it should be taken into account in order to calculate the optical parameter, namely the optical absorption length ($\ell_\beta = \beta^{-1}$).

In the experiments, quantitative measurements were carried out over a wide frequency range varying from 4000 to 400 cm^{-1}. Thus, β calculated from the transmission FT-IR spectrum of the outdoor patina layer varies significantly from β = 1 ÷ 3 cm^{-1} in the region of weak absorption (2500-1300 cm^{-1}) to its maximum values β = 38 ÷ 40 cm^{-1} at characteristic bands [46] of brochantite $Cu_4(OH)_6SO_4$, i.e. at 3388 cm^{-1} and 1123 cm^{-1}. As a result, the optical absorption length ranges from ℓ_β = 250 μm to ℓ_β = 1 cm.

The same analysis for the indoor patina layer characterized by low absorption result in the absorption length variation from ℓ_β = 2400 μm to ℓ_β = 1.5 cm.

As it can be clearly seen from the above results $\ell_p << \ell_\beta$ over the all frequency range used, thus both the outdoor and indoor layers of our samples can be considered as an optically transparent [45].

3.3 Depth Profiling Analysis of the Patina

3.3.1 Frequency dependence of the PA signal

According to the RG theory [45] the dependence of the PA signal (S) on β and f can be predicted regarding the relative magnitudes of the thermal diffusion length μ as compared to the sample thickness ℓ and the optical absorption length ℓ_β. Two well known dependences can be considered [45]:

$$S = \frac{I_0(1-e^{-\beta\ell})}{\rho_b C_b \omega \mu_b}, \quad \text{for the thermally thin sample } (\mu > \ell) \qquad (8)$$

where I_0 is the incident light flux, ρ_b, C_b and μ_b are the density, the specific heat and the thermal diffusion length of the backing material, respectively.

For the thermally thick samples ($\mu < \ell$):

$$S = \frac{I_0(1-e^{-\beta\mu})}{\rho C \omega \mu} \qquad (9)$$

It has be shown [45] that the frequency dependence of the PA signal varies from $S \sim f^{-1}$ for the optically transparent ($\ell < \ell_\beta$) thermally thin solids to $S \sim f^{-1.5}$ for the optically opaque ($\ell > \ell_\beta$) thermally thick samples.

The later case is of special importance for the spectroscopic studies as it can result in the photoacoustic saturation and corresponding loss of spectral detail.

3.3.2 A power-index method to study photoacoustic saturation

Thus, it would be helpful to calculate the power index n spectrum of the PA signal frequency dependence $S \sim f^{n}$ and to compare it with the normal FT-IR PAS spectrum. It can be done for each point of the FT-IR spectra obtained with the use of two different OPD velocities υ_1 and υ_2 by simple operation:

$$n = \frac{\mathrm{Log}(S_1/S_2)}{\mathrm{Log}(\upsilon_1/\upsilon_2)} \qquad (10)$$

This analysis can be performed for any number of the OPD velocities used indicating the variations in n (which is actually the slope of the PA signal log-log dependence on f or υ) due to the changes in the PA signal formation conditions.

Figure 19 shows the FT-IR spectra of the outdoor side of patinated sample collected with the use of different OPD velocities and 8 cm^{-1} resolution.

The form of each spectrum is similar to that of brochantite [46] $Cu_4(OH)_6SO_4$ except of some peaks whose origin will be discussed in the following sections. The FT-IR PAS signal decreases with increasing the OPD velocity.

A log-log frequency dependence of the FT-IR PAS signal for three intensive peaks in OH absorption band of brochantite $Cu_4(OH)_6SO_4$ presented in Fig.20 shows the variations in the slope of the lines from low to high OPD velocities. The right scale in Fig. 20 presents the ratios of the peaks at 3401 cm^{-1} to those at 3591 cm^{-1} and 3658 cm^{-1}. As it can be clearly seen from this figure these peaks have different frequency dependencies inspite of the fact that they are due to the same component of the patina.

Figure 21 shows the example of the application of the power-index method described above to analysis of the FT-IR spectrum of the patinated sample. Here the power index n of the frequency dependence has been calculated with the use of low OPD velocities from 0.101 to 0.253 cm/s. As it can be stated from this figure, the form of the power-index spectrum follows that of the normal FT-IR PAS spectrum in all the wavenumbers range used: from 4000 to 400 cm^{-1}. It ranges from n = - 1.5 in the region of low absorption (near 2500 cm^{-1}) to n = -1.1 at the most intensive peaks of brochantite $Cu_4(OH)_6SO_4$, i.e. at 3401 cm^{-1} and in the region of SO_4 absorption: 1200 - 400 cm^{-1}.

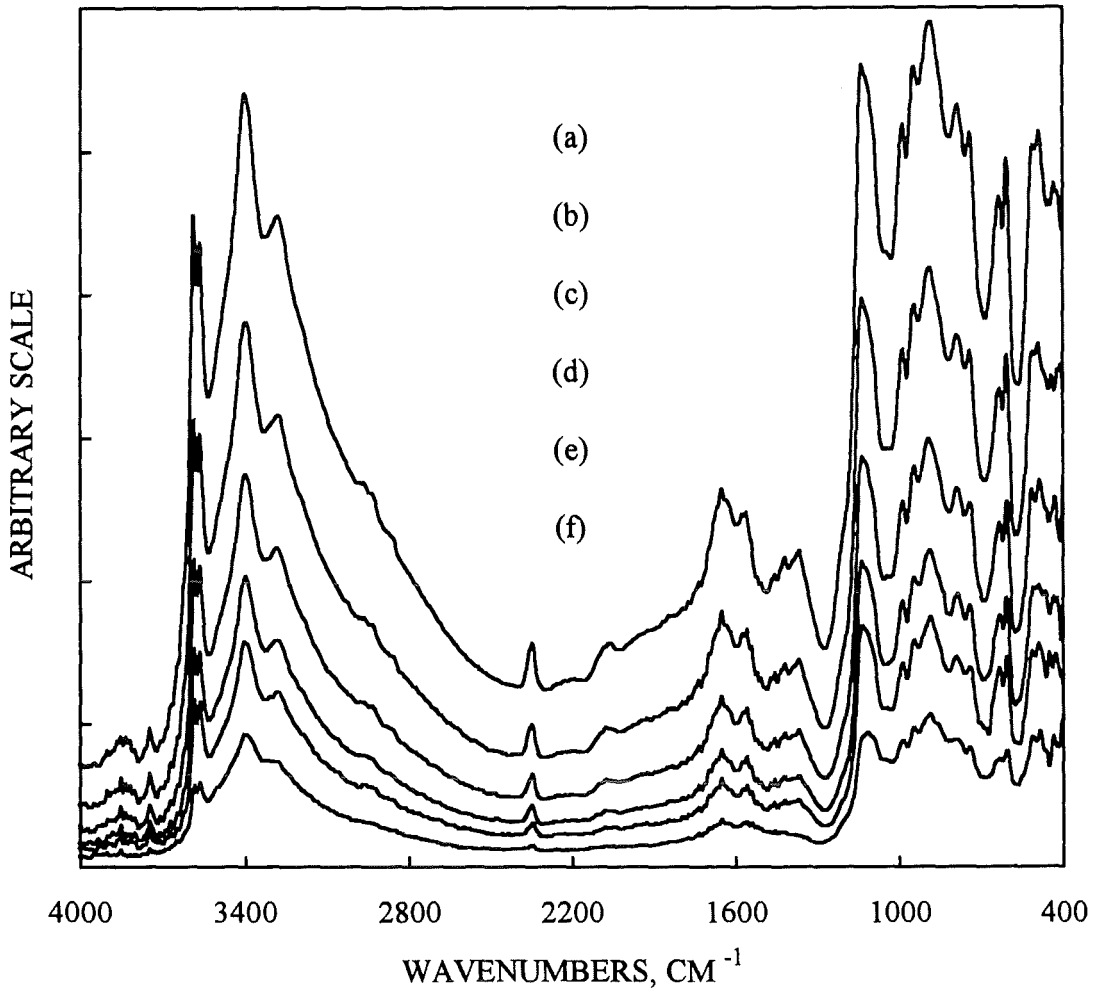

Fig.19 FT-IR PAS spectra of the outdoor side of patinated sample obtained with the use of the following OPD velocities: 0.101 cm/s (a), 0.139 cm/s (b), 0.190 cm/s (c), 0.253 cm/s (d), 0.316 cm/s (e) and 0.475 cm/s (f). Spectral resolution: 8 cm^{-1}.

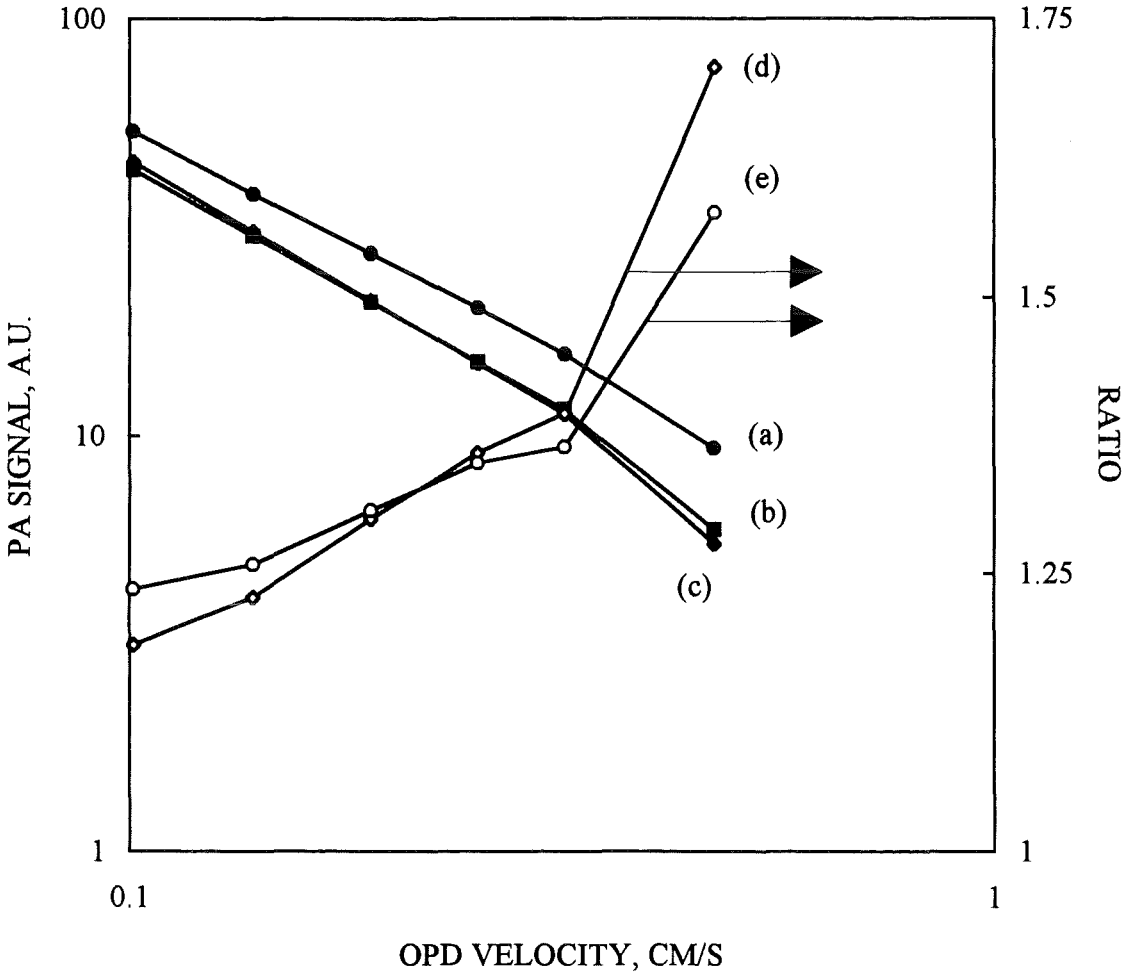

Fig.20 A log-log plot of the PA signal vs. the OPD velocity for the most intensive OH lines of brochantite $Cu_4(OH)_6SO_4$: at 3401 cm^{-1} (a), 3591 cm^{-1} (b) and 3568 cm^{-1} (c). The right scale represents the same dependence for the ratios of these peaks: (PA at 3401 cm^{-1})/(PA at 3591 cm^{-1}) - (d), and (PA at 3401 cm^{-1})/(PA at 3568 cm^{-1}) - (e).

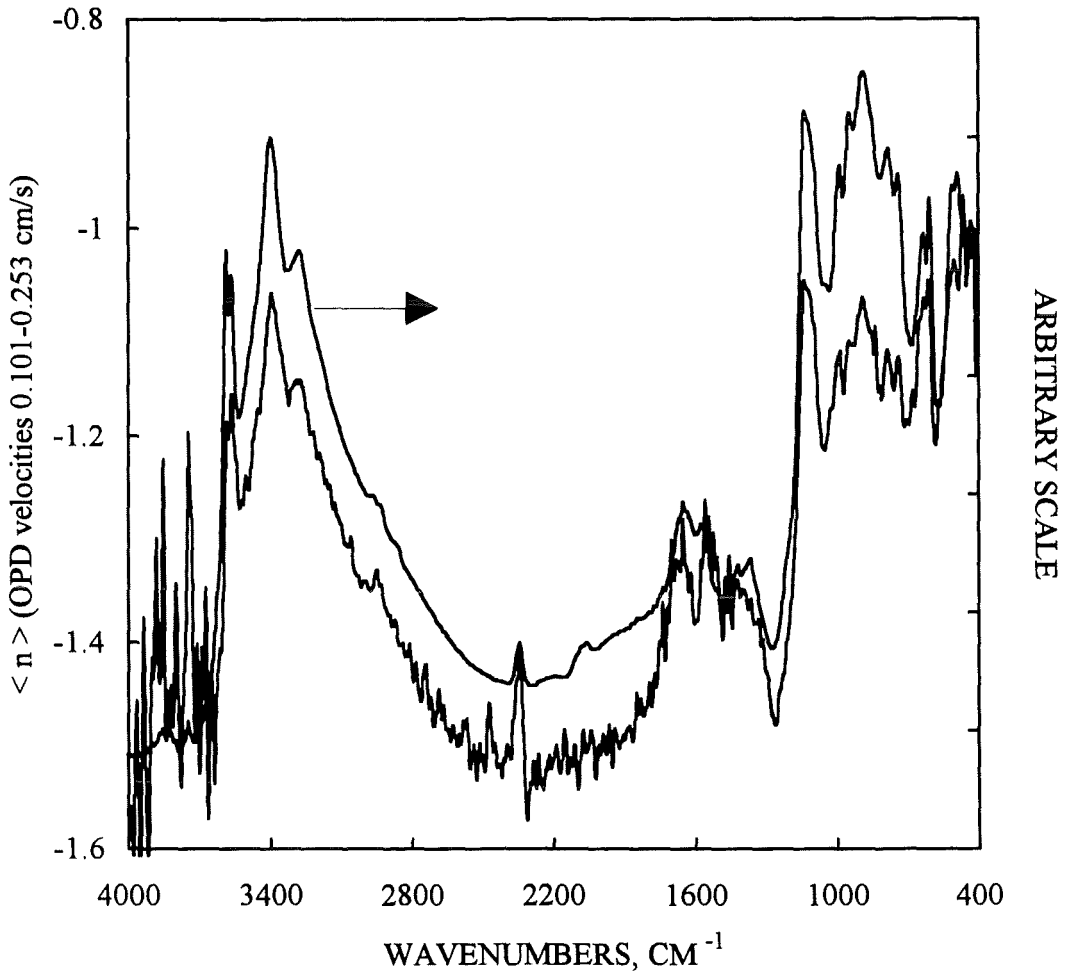

Fig.21 FT-IR PAS spectrum of the outdoor side of patinated sample obtained with the OPD velocity of 0.101 cm/s (right scale) and the mean power index < n > spectra of the dependence PA signal ~ f^n calculated with the use of the OPD velocities from 0.101 cm/s to 0.253 cm/s (left scale), as explained in the text.

This wavenumber dependence of n indicates that our sample is optically transparent and thermally thin at the most intensive absorption bands. It can be also stated that in the case of the patinated sample we are far from the photoacoustic saturation which occurs for optically opaque and thermally thick solids and is characterized by n = - 1.5 [45]. Note, that inspite of the fact that in these high absorption regions the PA signal also depends on the thermal properties of the backing material (Cu) its influence is not significant.

In contrast to the previous case, in the low absorption region (2800 cm^{-1} - 2000 cm^{-1}) an optically opaque and thermally thick Cu backing dominates in the formation of the PA signal which result in another frequency dependence with n = - 1.5.

With increasing the OPD velocity υ (and the modulation frequency f) the ratio μ/ℓ changes permanently from $\mu/\ell < 1$ at low OPD velocities: 0.101-0.190 cm/s to $\mu/\ell \sim 1$ at high OPD velocities: 0.253-0.475 cm/s (Table I). Corresponding variations in the mean power index $< n >$ calculated for these two characteristic regions of υ can be clearly seen in Fig.22.

The most intensive peak at 3401 cm^{-1} shows the changes in power index from $< n > = - 1.05$ at low υ to $< n > = - 1.15$ at high OPD velocities. Further increase in υ (above 0.475 cm/s) will result in the case of the thermally thick sample $\mu/\ell > 1$ which is characterized by $< n > = - 1.5$ (eq.(8)). This dependence of $< n >$ on the modulation frequency is evident from the slope changes in Fig. 20(a) with increasing the OPD velocity.

Let us note the difference between the frequency dependence of $< n >$ for the peaks at 3591 cm^{-1} and 3568 cm^{-1} with respect to that for the peak at 3401 cm^{-1} (Fig.22). As it can be stated from the comparison of two curves behaviour in the region of fundamental vibrational frequencies of OH between 3600 cm^{-1} and 3200 cm^{-1}, at high values of υ the power index n drops drammatically for the two first OH bands reaching the value of $< n > = - (1.25 \div 1.30)$.

In addition, the form of the power index spectrum no more follows that of the FT-IR PAS as these two OH peaks are absent in the right-hand curve of Fig.22. This is probably due to the difference in cristalline structure of brochantite $Cu_4(OH)_6SO_4$ along the depth of the patina layer resulting in decrease of the relative intensities of free non-hydrogen bonded OH lines usually identified as O_5H and O_6H, respectively [46].

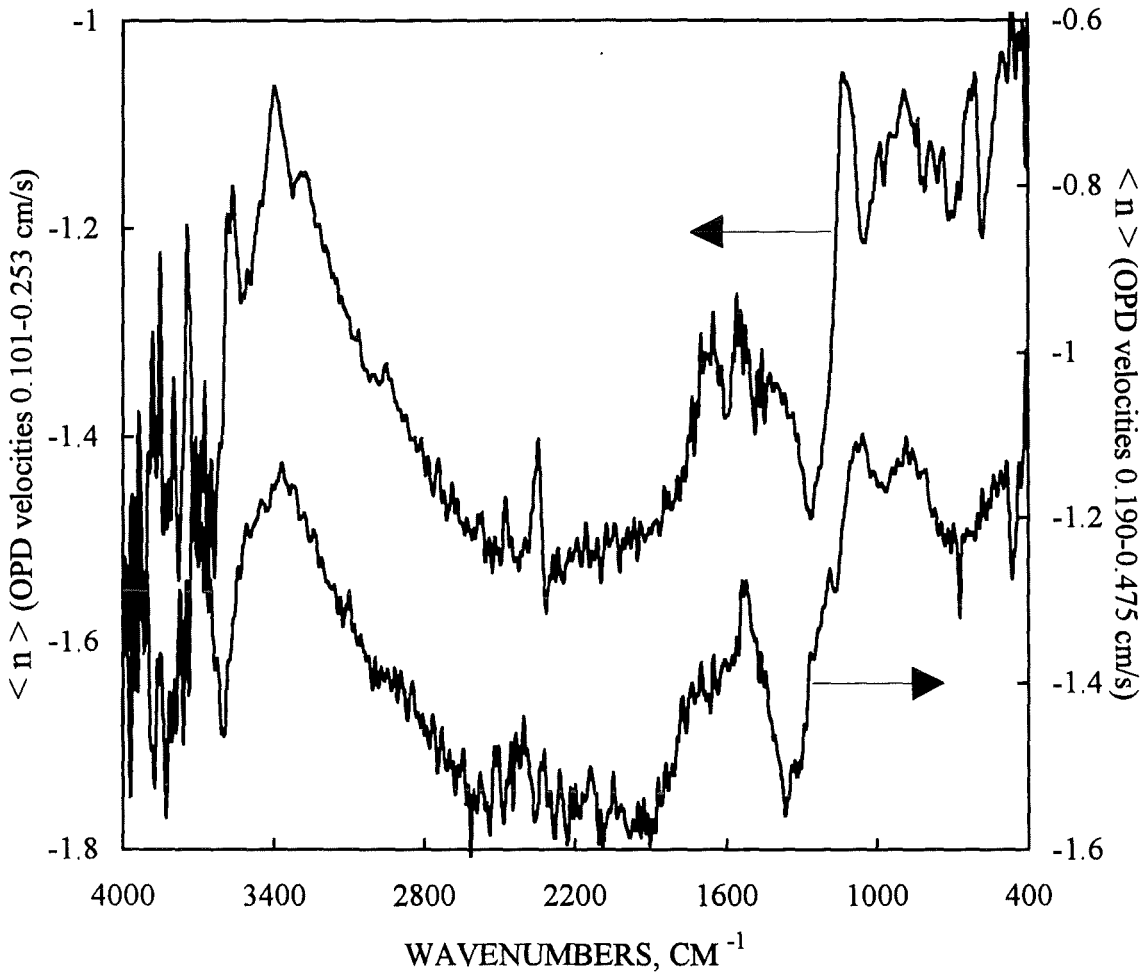

Fig.22 The mean power index < n > spectra for the outdoor side of patinated sample calculated with the use of the OPD velocities from 0.101 cm/s to 0.253 cm/s (left scale) and from 0.190 cm/s to 0.475 cm/s (right scale). Note the right and left scales displacement.

3.3.3 Spectral resolution

We also noted that in some cases the power index < n > spectrum shows better peaks resolution than the normal FT-IR spectrum (Fig.23). It may be due to better sensitivity of n to the changes in μ and β and, correspondingly, in the regime of the PA signal formation compared to that of the PA amplitude.

This advantageous feature of the power index method allows to resolve even the peaks which are not seen in the FT-IR PAS spectrum. As an example, the < n > spectrum in Fig.21 shows the presence of several peaks between the most intensive OH bands discussed above. These peaks have been identified to be due to another patina components - antlerite $Cu_3(OH)_4SO_4$ and copper (II) nitrite $Cu_4(OH)_6(NO_3)_2$ (see also next section).

Having based on the results discussed above we concluded that the application of this simple method of the FT-IR data presentation leads to the additional important information which can not be obtained by using the standard FT-IR PAS data processing procedure. We used this method in the following spectroscopic analysis of the patina.

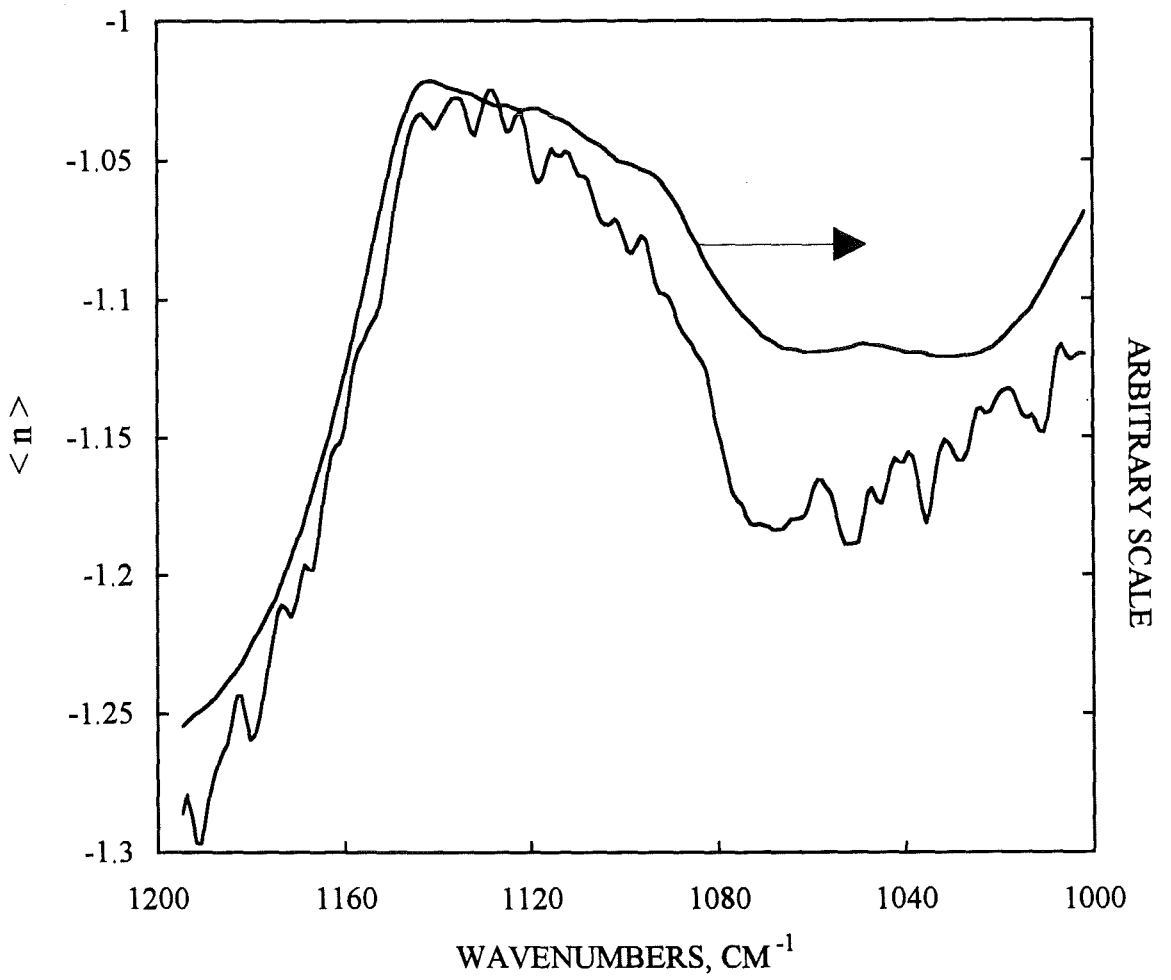

Fig.23 The mean power < n > spectrum for the outdoor side of patinated sample calculated with the use of low OPD velocities: 0.101-0.139 cm/s (left scale) and the FT-IR spectra recorded at OPD velocity of 0.101 cm/s in the region of sulfate internal optical mode frequencies (ν_3 region). The < n > spectrum shows more clearly the fine structure of the broad peak from 1160 cm^{-1} to 1080 cm^{-1}.

3.4 FT-IR PAS Spectra For the Outdoor Patina Layer

3.4.1 OH absorption

In two following sections we present the results of the FT-IR PAS method application to the identification of the main patina components on both the outdoor and indoor sides of our samples. For these purposes we used 4 cm^{-1} resolution spectra collected over 1024 scans at different OPD velocities.

Figure 24 shows the FT-IR PAS spectra measured on the outdoor side of patinated sample. As it can be clearly seen from this figure there are three characteristic absorption regions:

- OH absorption region (3600-2800 cm^{-1}),
- intermediate absorption region close to water-vapour bands (1500-1300 cm^{-1})
- characteristic SO_4 absorption region (1200-400 cm^{-1}).

We used the OPD velocities range up to 1.27 cm/s as further increase in υ result in the FT-IR PAS signal too weak to be detected by our experimental set up.

Inspite of the fact that before each measurement we purged the PA cell with the sample by dry nitrogen some traces of atmospheric CO_2 are still present on the FT-IR PAS spectra (the peak at 2200 cm^{-1}). The intensity of the water-vapour bands near 1600 cm^{-1} has been decreased by a factor of 3 by using the purging procedure. The absorption bands in this region are due to the water-vapours remain in the patina layer characterized by very high porosity [4-11].

For the following analysis we divided the whole spectral range into three parts regarding to the absorption character.

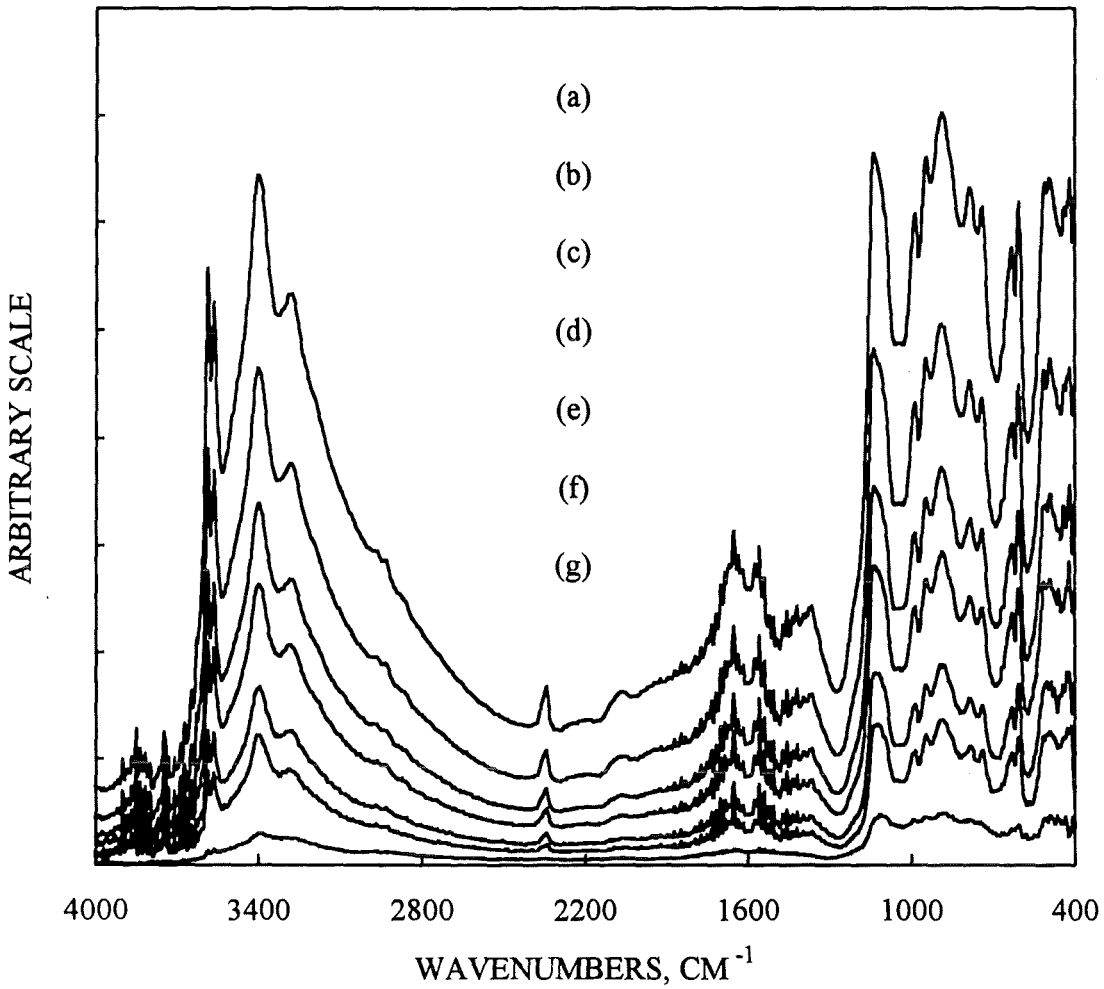

Fig.24 FT-IR PAS spectra of the outdoor side of patinated sample obtained with the use of the following OPD velocities: 0.139 cm/s (a), 0.190 cm/s (b), 0.253 cm/s (c), 0.316 cm/s (d), 0.475 cm/s (e), 0.633 cm/s (f) and 1.27 cm/s (g). Spectral resolution: 4 cm^{-1}.

The shape of the FT-IR PAS spectra in OH absorption region is quite similar to that of brochantite $Cu_4(OH)_6SO_4$ and two other basic copper sulfates: $Cu_4(OH)_4OSO_4$ and antlerite $Cu_3(OH)_4SO_4$. The fundamental vibration frequencies for OH were found to occur over the range 3600-3200 cm^{-1} depending on the degree of H-bonding.

Figure 25(a) shows a clearly resolved multiple structure in the spectrum of the outdoor patina layer indicating the three distinct classes of hydroxyl groups known to exist in the brochantite [46] $Cu_4(OH)_6SO_4$. In order to increase the peaks resolution we also used the power index spectra calculated by using the low OPD velocities (Fig. 25(b)).

The sharp peaks at 3590 and 3570 cm^{-1} obtained on the normal FT-IR PAS spectra and repeated on $< n >$ spectrum at low OPD velocities are close to that reported earlier by Secco [46] for brochantite $Cu_4(OH)_6SO_4$: 3596 and 3572 cm^{-1}, respectively. They are assigned to free non-hydrogen bonded OH. The slightly broader band centred at 3395 cm^{-1} with fine structure is consistent with the different degrees of hydrogen bridging [46].

The results of the same analysis of different OH frequencies performed for other most common patina components - copper sulfate [46] $Cu_4(OH)_4OSO_4$, antlerite [46] $Cu_3(OH)_4SO_4$, copper (II) nitrite [47] $Cu_4(OH)_6(NO_3)_2$ and copper carbonate [48] $Cu_2CO_3(OH)_2 \cdot H_2O$ - are presented in Table II.

The following characteristic bands which are different from that of brochantite $Cu_4(OH)_6SO_4$ were found for two other basic copper sulfates: the OH stretching frequency of 3488 cm^{-1} and the free OH band at 3580 cm^{-1} for antlerite $Cu_3(OH)_4SO_4$; and the dehydroxylated frequency at 3186 cm^{-1} for copper sulfate $Cu_4(OH)_4OSO_4$.

For the copper (II) nitrite $Cu_4(OH)_6(NO_3)_2$ we recorded the fundamental OH frequencies 3551 cm^{-1}, 3475 cm^{-1} and 3415 cm^{-1}. The third of them is close to the corresponding OH frequency of brochantite $Cu_4(OH)_6SO_4$.

The presence of copper carbonate $Cu_2CO_3(OH)_2 \cdot H_2O$ was identified by the weak absorption band at 3320 cm^{-1} as another characteristic band at 3410 cm^{-1} is close to that of brochantite $Cu_4(OH)_6SO_4$ and copper (II) nitrite $Cu_4(OH)_6(NO_3)_2$ (Table II).

Figures 25(b) and 25(c) illustrate the changes in frequency dependence of different peaks in OH absorption region. As it has been noted earlier, the power index $< n >$ for the two first non-hydrogen bonded OH bands drops significantly reaching the value of $< n > = -1.5$ at high OPD velocities (thermally thick sample) while for other bands it remains at the level of $< n > = -1.4$.

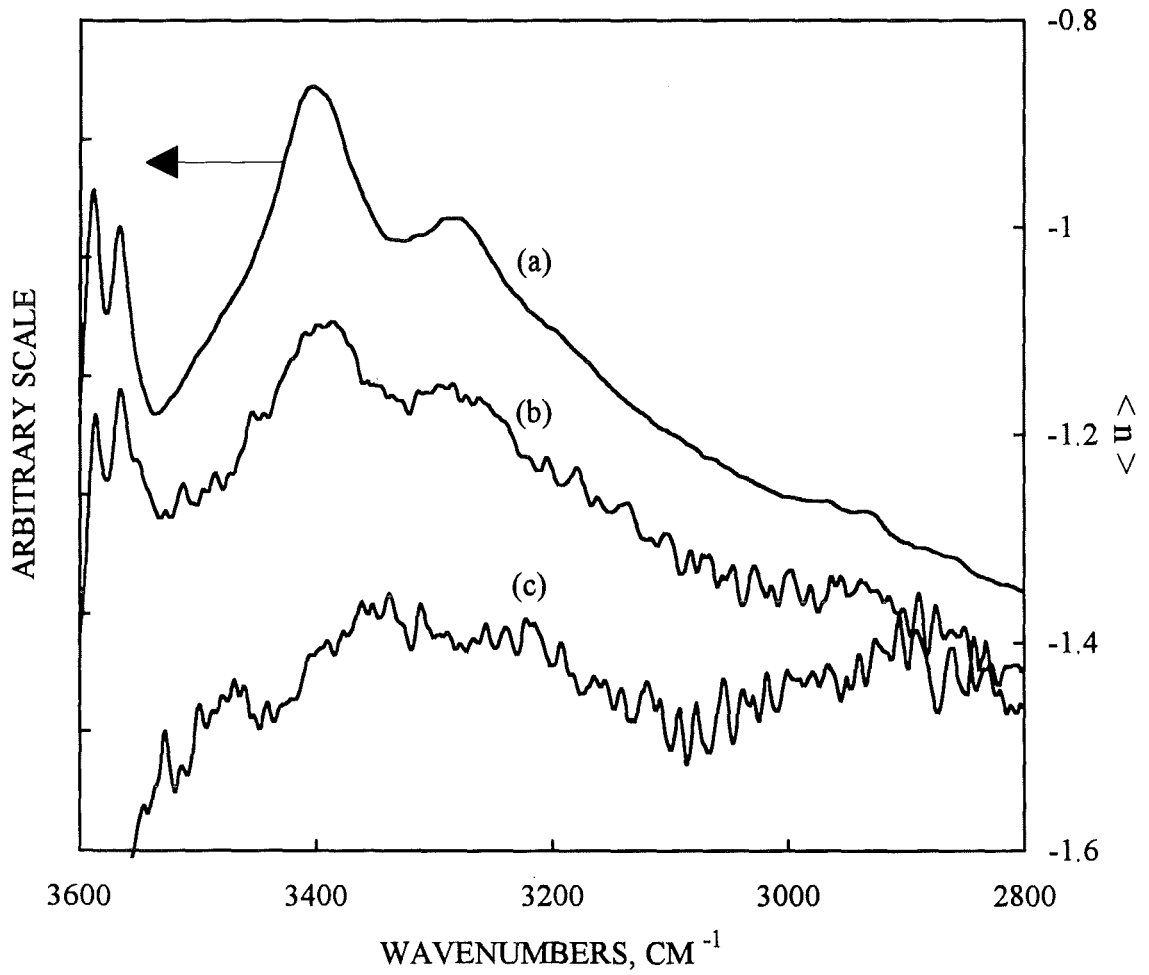

Fig.25 FT-IR spectrum of the outdoor side of patinated sample recorded at OPD velocity of 0.139 cm/s in the region of OH absorption (a) and the mean power < n > spectra calculated with the use of low OPD velocities: 0.139-0.190 cm/s (b) and high OPD velocities: 0.633-1.27 cm/s (c).

Table II

Identification of the IR frequencies (cm^{-1}) of the outdoor side of patinated sample measured by using the FT-IR PAS for region 3600-3200 cm^{-1}.

Patina layer	Brochantite[a] $Cu_4(OH)_6SO_4$	Antlerite[a] $Cu_3(OH)_4SO_4$	Copper sulfate[a] $Cu_4(OH)_4OSO_4$	Copper (II) nitrite[b] $Cu_4(OH)_6(NO_3)_2$	Copper carbonate[c] $Cu_2CO_3(OH)_2H_2O$
3590	3596	3588	3596	-	-
3580*	-	3580	-	-	-
3570	3572	-	3572	-	-
3551*	-	-	-	3550	-
3488*	-	3488	-	-	-
3478*	-	-	-	3475	-
3414	3412	-	-	3415	3410
3395	3393	-	3390	-	-
3320*	-	-	-	-	3320
3275	3272	-	3273	-	-
3185*	-	-	3186	-	-

[a] From Ref. 46.
[b] From Ref. 47.
[c] From Ref. 48.
* Frequencies obtained from the power index < n > spectra at low OPD velocities (0.139-0.190 cm/s).

This fact verified several times allowed us to conclude the inhomogeneity in OH-containing substances depth distribution and/or depth changes in their crystalline structure resulting in variation in the thermal diffusivity.

3.4.2 Intermediate absorption region

The FT-IR PAS spectrum and the power index spectrum in this region are presented in Fig.26. We recordered several peaks corresponding to azurite $Cu_2(CO_3)_2(OH)_2$ at 1419 cm^{-1}, precipitated cupric carbonate $CuCO_3$ at 1395 cm^{-1} and malachite $Cu_2CO_3(OH)_2$ at 1388 cm^{-1}.

These bands are in good agreement with those measured by Nassau et al. [9] for the same minerals by using ordinary IR transmission spectra: 1416 cm^{-1} , 1400 cm^{-1} and 1391 cm^{-1}, respectively.

The most intensive peak in this region situated at 1375 cm^{-1} has been mentioned in previous studies [9] but remained unidentified. We suggest the presence of copper (II) fluoride $CuF_2 \cdot xH_2O$ which has strong absorption band [48] at 1375 cm^{-1}. This patina component can be present due to different atmospheric particles incorporated into copper patina.

In addition to the FT-IR PAS spectrum, the power index spectrum (Fig.26(b)) shows the presence of two clearly resolved peaks at 1320 cm^{-1} and 1347 cm^{-1} which we are not able to identify.

The form of the $< n >$ spectrum follows that of the FT-IR PAS and the mean value $< n > = -1.4$ indicates the regime close to optically opaque and thermally thick sample due to the presence of Cu backing.

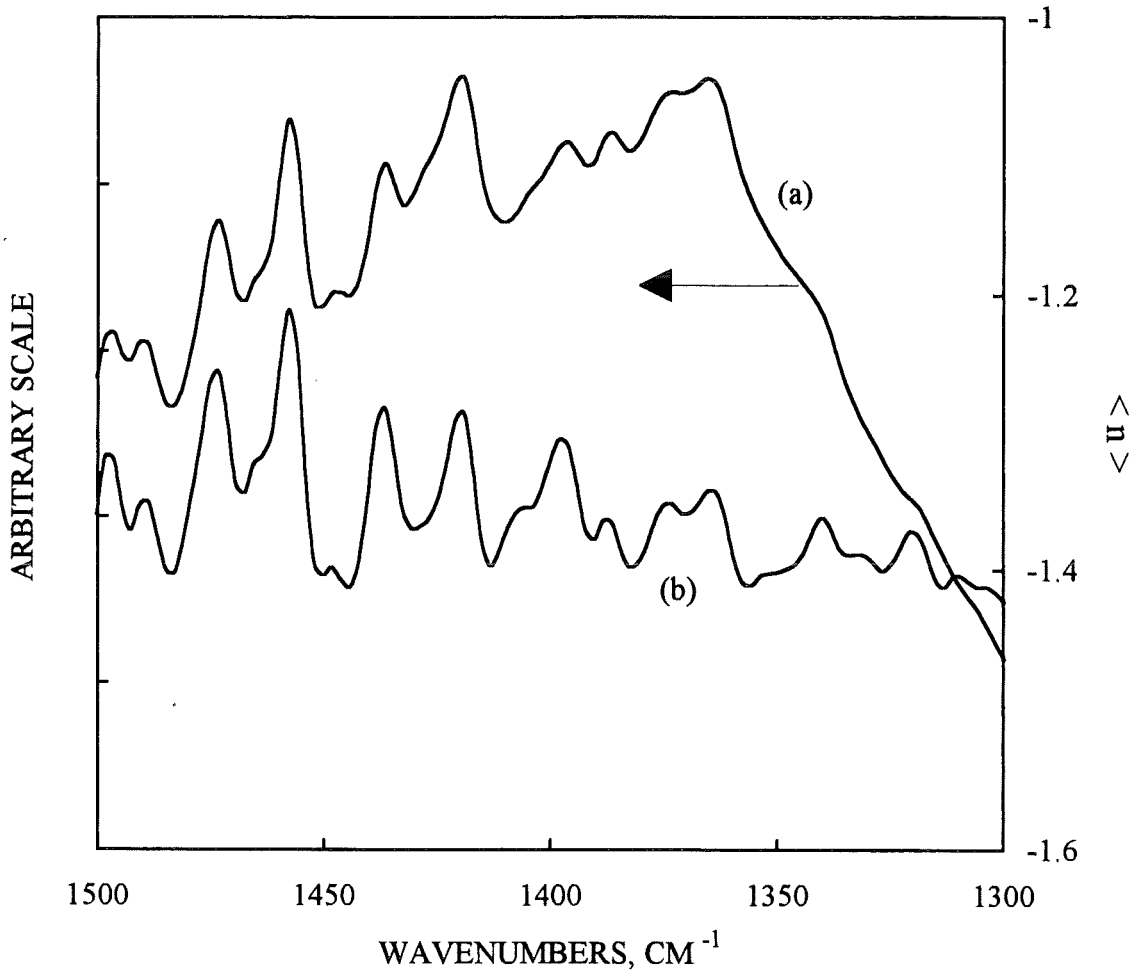

Fig.26 FT-IR spectrum of the outdoor side of patinated sample recorded at OPD velocity of 0.139 cm/s in the intermediate absorption region (a) and the mean power < n > spectrum calculated with the use of low OPD velocities: 0.139-0.190 cm/s (b).

3.4.3 SO_4 absorption

In this region the general form of the FT-IR PAS spectra shown in Fig. 27(a) is similar to that of brochantite [46] $Cu_4(OH)_6SO_4$ with a lot of additional features due to the presence of another patina components. In this SO_4 absorption region we recorded 33 peaks both using the FT-IR PAS and the power index spectra. The results of the IR frequencies identification are presented in Table III.

Except of brochantite $Cu_4(OH)_6SO_4$, we found the presence of copper sulfate $Cu_4(OH)_4OSO_4$ (identified by the individual characteristic absorption bands at 1140 cm^{-1} and 550 cm^{-1}), antlerite $Cu_3(OH)_4SO_4$, copper oxysulfate $Cu_3O_2SO_4$, copper (II) nitrite $Cu_4(OH)_6(NO_3)_2$ and basic cupric carbonate $Cu_2CO_3(OH)_2 \cdot H_2O$ (Table III).

The power index < n > spectrum calculated for the low OPD velocities (Fig. 11b) follows the shape of the normal FT-IR PAS spectrum and fluctuates between $< n > = -1.1$ and $< n > = -1.2$. As it has been noted above (Sect. 2) this wavenumber dependence of < n > indicates that our sample is optically transparent and thermally thin in this region.

It should be pointed out that the above analysis is not complete as we identified only the most common components of the patina. Several peaks both in the normal FT-IR PAS spectrum and in power index < n > spectrum remain unidentified. They are due to the presence of other patina components which number can reach 70 according to Graedel et al. [4].

Table III

Identification of the IR frequencies (cm^{-1}) of the outdoor side of patinated sample measured by using the FT-IR PAS for region 1150-400 cm^{-1}.

Patinated sample	Brochantite[a] $Cu_4(OH)_6SO_4$	Copper sulfate[a] $Cu_4(OH)_4OSO_4$	Antlerite[a] $Cu_3(OH)_4SO_4$	Copper oxysulfate[b] $Cu_3O_2SO_4$	Copper (II) nitrite[c] $Cu_4(OH)_6(NO_3)_2$	Basic cupric carbonate[d] $Cu_2CO_3(OH)_2H_2O$
1141	-	1140	-	-	-	-
1123	1123	-	-	-	-	-
1119	1117	1120	-	-	-	-
1096	-	-	-	-	-	1096
1050	-	-	-	1050	-	1050
989	990	-	988	-	-	-
947	945	945	-	-	-	-
890	-	-	-	-	890	-
882	878	-	880	-	878	880
851	850	850	850	-	-	-
818	-	-	-	-	-	817
809	-	-	807	-	809	-
797	-	-	796	-	-	-
781	780	779	-	-	780	-
752	-	-	750	-	-	750
668	-	670	666	668	667	-
649	-		-	648	-	-
641	640	640	640	642	-	-
631	630	630	-	630	-	-
608	-	-	-	608	-	-
578	-	-	-	576	-	580
573	-	-	-	575	-	-
551	-	550	-	-	-	-
518	-	-	518	-	-	-
513	513	514	-	-	-	-
509	-	-	-	-	510	-
485	485	484	-	-	-	-
471	470	470	-	-	-	-
464	463	462	-	-	-	-
458	-	-	457	-	-	-
453	-	-	-	-	454	-
431	-	-	-	-	-	430
421	420	420	420	-	-	-

[a] From Ref. 46; [b] From Ref. 49; [c] From Ref. 47; [d] From Ref. 48.

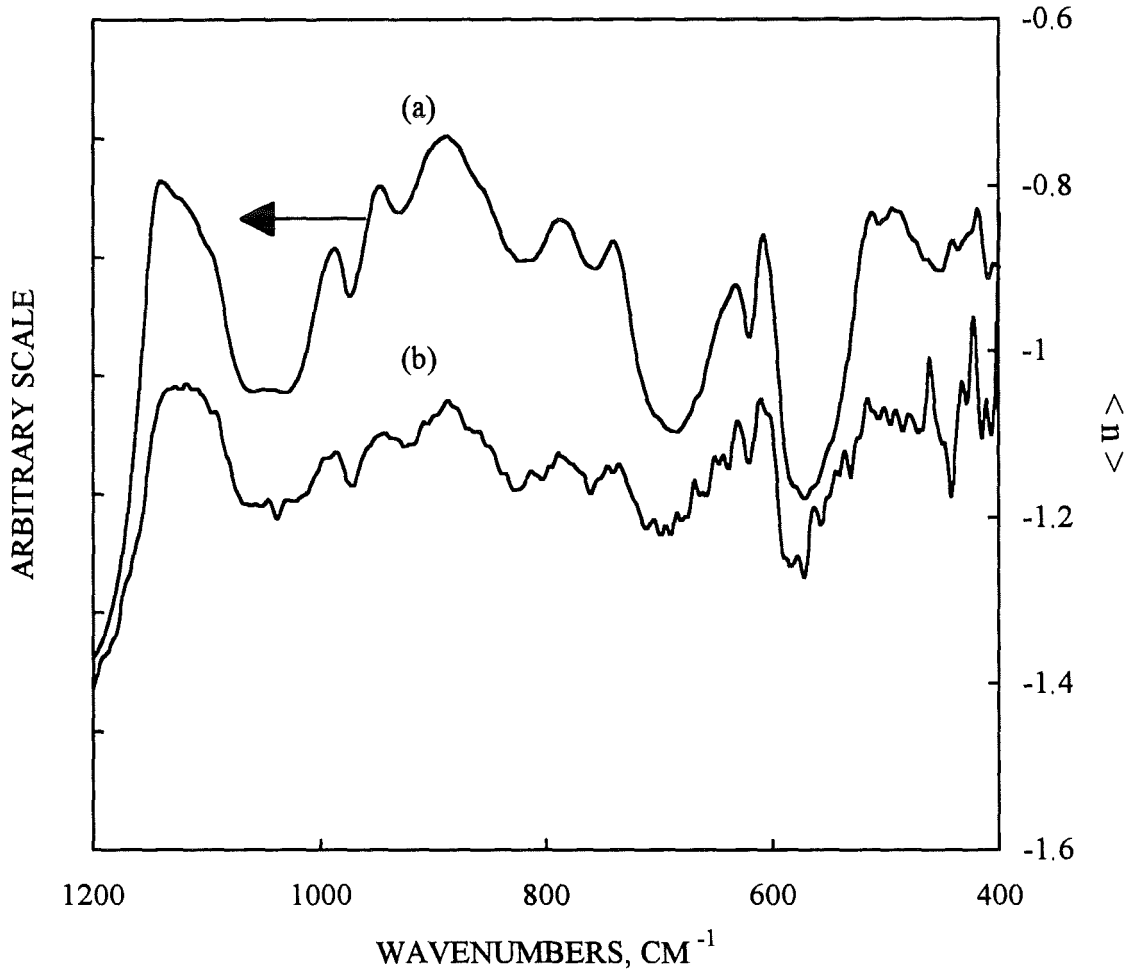

Fig.27 FT-IR spectrum of the outdoor side of patinated sample recorded at OPD velocity of 0.139 cm/s in the region of SO_4 absorption (a) and the mean power < n > spectrum calculated with the use of low OPD velocities: 0.139-0.190 cm/s (b).

3.5 FT-IR PAS Spectra For the Indoor Patina Layer

The FT-IR PAS spectra for OH and SO_4 absorption regions obtained on the indoor side of patinated sample are presented in Figs. 28 and 29, respectively.

The PA signal was very weak for this indoor side due to low optical absorption which is at least 10 times lower than that for the outdoor side. Based on the FT-IR spectra recorded at low OPD velocities we found the presence of brochantite $Cu_4(OH)_6SO_4$, antlerite $Cu_3(OH)_4SO_4$, and, possibly, basic cupric carbonate $Cu_2CO_3(OH)_2 \cdot H_2O$. These components are typical for the initial patina layer grown in marine atmosphere [10]. We were not able to perform more precise bands identification due to the low signal-to-noise ratio in these spectra.

We also noted the presence of several unidentified peaks at 2900 and 2800 cm^{-1} which appear both on the outdoor and indoor sides of our patinated sample (Figs. 19 and 24). These peaks are more pronounced on the indoor side and are supposed to be due to the organic components of the patina.

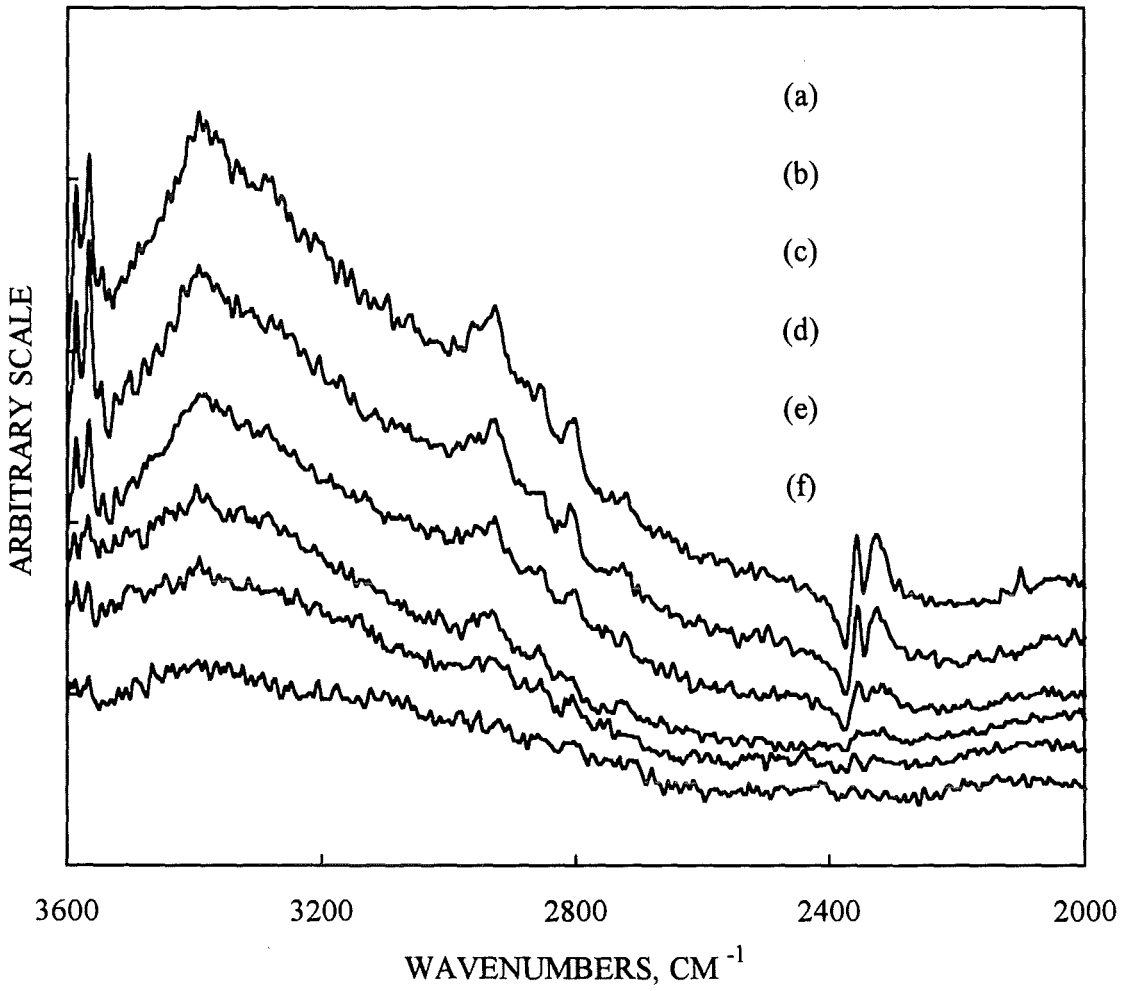

Fig.28 FT-IR PAS spectra of the indoor side of patinated sample in the region of OH absorption obtained with the use of the following OPD velocities: 0.101 cm/s (a), 0.139 cm/s (b), 0.190 cm/s (c), 0.253 cm/s (d), 0.316 cm/s (e) and 0.475 cm/s (f). Spectral resolution: 4 cm^{-1}.

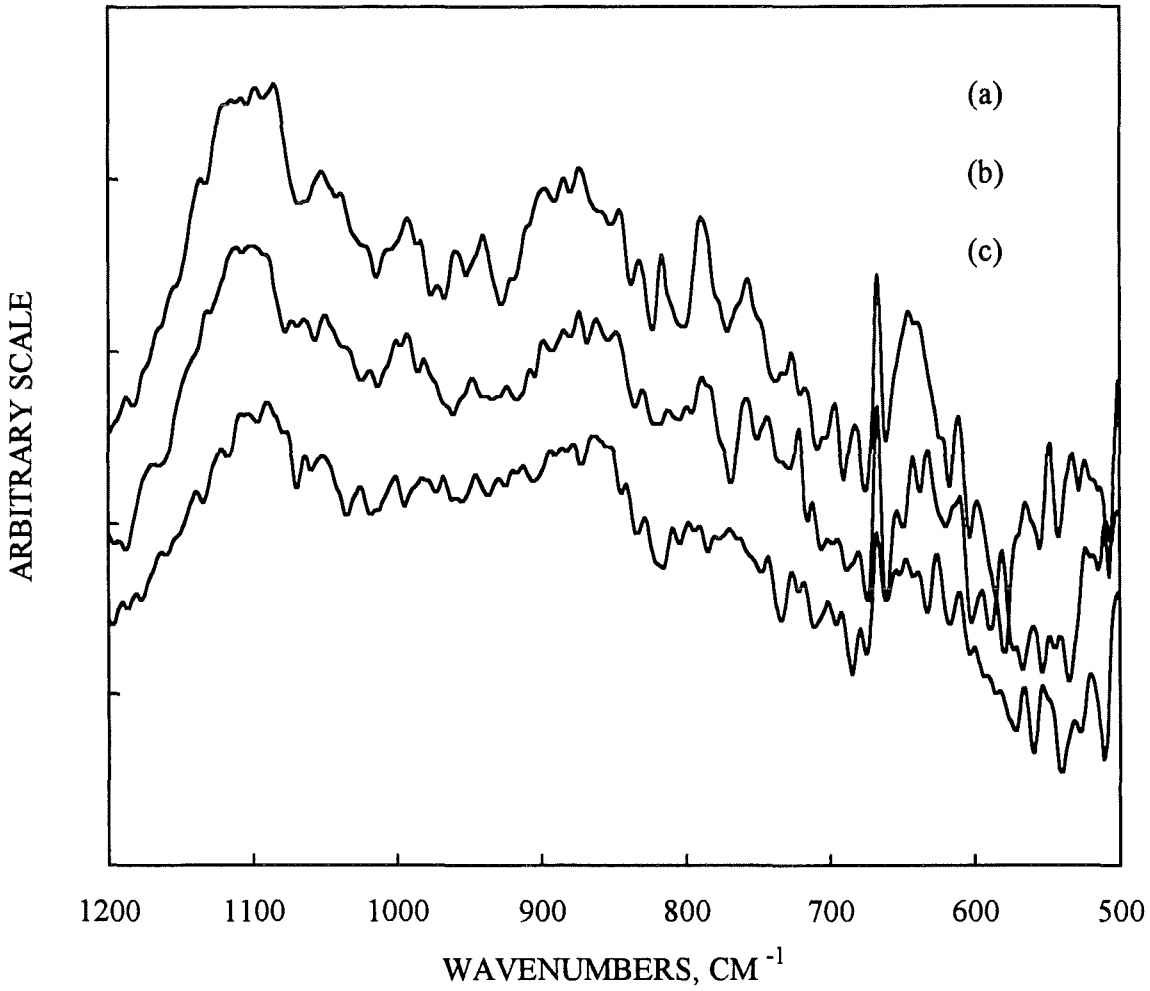

Fig.29 FT-IR PAS spectra of the indoor side of patinated sample in the region of SO_4 absorption obtained with the use of the following OPD velocities: 0.101 cm/s (a), 0.139 cm/s (b) and 0.190 cm/s (c). Spectral resolution: 4 cm^{-1}.

Summary to Chapter 3

We have presented in this Chapter the results of the FT-IR PAS technique application in natural copper patina analysis. It has been shown that this method is a useful tool for nondestructive testing of these corrosion layers allowing to obtain quantitative important information about the patina layer components and structure.

By using this FT-IR PAS method we have identified about 10 different patina components including some new components such as copper (II) fluoride CuF_2xH_2O which have been not detected previously in the patina.

The depth profiling capability of the FT-IR PAS method allowed us to determine the degree of photoacoustic saturation of the spectral bands and the depth distribution of the patina components. A new power index method has been proposed for these purposes.

Based on the results obtained we concluded that the FT-IR PAS technique compares favourably with more common approaches of patina examination which are more expensive, usually destructive and requires special sample preparation.

Conclusions

We described in the present work the results of the application of modern nondestructive photothermal and photoacoustic methods to study of one of the important environmental samples - copper protective corrosion layer (patina). Two different experimental techniques were used for these purposes: the photothermal beam deflection (PBD) method and Fourier transform infrared photoacoustic spectroscopy (FT-IR PAS).

A new photothermal approach in the studies of patinated copper layers was proposed. A noncontact and nondestructive PBD method was used for the characterisation of thermal properties of patinated copper samples from the roof of the Stockholm City Hall. Quantitative measurements of thermal diffusivity and layer thickness performed on both the outdoor and indoor sides of patinated samples show a significant difference in their thermal properties. Photothermal images obtained for both sides of patinated samples were used for the analysis of patina layer surface morphology and the microstructure of includings.

The FT-IR PAS has proved to be a useful tool for nondestructive testing of the patina. By using this method we have identified about 10 different patina components including some new components such as copper (II) fluoride CuF_2xH_2O which have been not detected previously in the patina. The depth profiling capability of the FT-IR PAS method allowed us to determine the degree of photoacoustic saturation of the spectral bands and the depth distribution of the patina components. A new power index method was proposed for these purposes.

Based on the results obtained we concluded that photothermal methods are very useful experimental techniques allowing to obtain important quantitative information in such studies. These methods thus compare favourably with more common approaches of environmental samples examination which are usually more expensive, destructive and requires special sample preparation.

Acknowledgements

The authors would like to thank Profs. H.-J. Ache (Director, Institut für Radiochemie, Forschungszentrum Karlsruhe), A. Vendl (University of Applied Arts in Vienna, Institute for Silicate Chemistry and Archaeometry) and B. Pichler (Vienna) for helpful discussions.

Thanks are also due to Drs. O. Zaitsev (Karlsruhe), H. Gantner (Karlsruhe) as well as due to O.Duebel, B.Seidel and B.Beck (Karlsruhe). Special thanks to Dr. J.Puhringer (Stockholm), who provided the sample material.

Appendix

A.1 A portable PBD-device for in-field measurements

As it has been shown in the previous Chapters, the photothermal methods are very useful tools for non-destructive and non-contact testing of environmental samples. Their sensitivity and relative simplicity allows researchers to perform quantitative express-analysis of the samples without any sample pre-treatment while the application of other traditional techniques requires special sample preparation. Further development of the photothermal methods application in such studies leads to the necessity of small portable device for in-field measurements. In addition to non-destructive and non-contact character of the photothermal methods such a device should be able to perform several important studies *„in vivo"*, i.e. without removal the sample from its historical place.

Figure 30 presents a schematic diagram of the measuring head (MH) of the proposed PBD-method based device for in-field measurements. The main parts of this MH are the same as in traditional laboratory PBD set up except of the system of the probe beam deflection amplification [50] based on the cylindrical mirror of defined diameter and the system of the probe beam deflection measurements [51]. The latter is based on four glass tubes coupled together and centred with respect to undeflected probe beam. The probe beam deflection will alter the light intensity in each tube which can be detected easily by using the system of four simple photodetectors installed in the data processing unit.

Several important features of this device should be considered:

- This MH is purely noncontact from the physical point of view. Only a small surface (about 0.8 cm^2) mechanical contact of the MH with the sample is needed.
- The MH contains only a very chip mechanical and optical parts without any electronics due to the special modern design of the system of the probe beam deflection detection. This fact allows to use the MH in any environments even containing high intensity electrical and magnetic fields, dangerous gases, etc. In addition, these circumstances reduce the prise for the MH unit and, correspondingly, for the whole device.
- This MH can be placed as far as it is needed from the data processing unit by using the optical fibers with low losses.

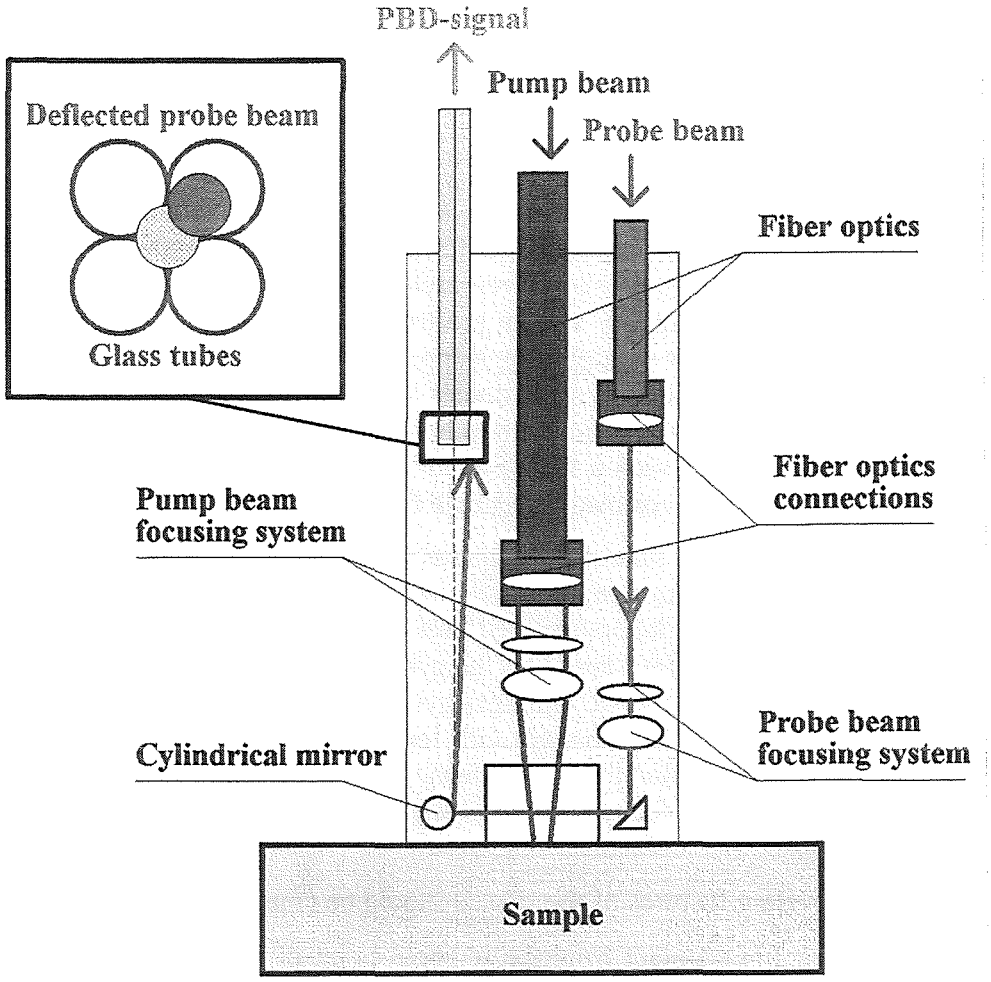

Fig. 30 A schematic diagram of the measuring head of the proposed portable device for in-field measurements based on the PBD method physical principles.

List of Figures

List of Tables

List of References

1. W. H. J. Vernon, J. Inst. Metals **52**, 93 (1933).
2. E. Mattsson, Br. Corros. J., **15**, 6 (1980).
3. P. D. Weil, P. Gaspar, L. Gulbransen, R. Lindberg and D. Zimmerman, In: *Science and Technology in the Service of Conservation* (N. S. Brommelle, G. Thomson Eds.), pp. 130-134. Int. Inst. for Conserv. of Historic and Artistic Works, London (1982).
4. T. E. Graedel, K. Nassau and J. P. Franey, Corros. Sci. **27**, 639 (1987).
5. J. P. Franey and M. E. Davis, Corros. Sci. **27**, 659 (1987).
6. K. Nassau, P. K. Gallagher, A. E. Miller and T. E. Graedel, Corros. Sci. **27**, 669 (1987).
7. R. L. Opila, Corros. Sci. **27**, 685 (1987).
8. A. J. Muller and C. McCrory-Joy, Corros. Sci. **27**, 695 (1987).
9. K. Nassau, A. E. Miller and T. E. Graedel, Corros. Sci. **27**, 703 (1987).
10. T. E. Graedel, Corros. Sci. **27**, 721 (1987).
11. T. E. Graedel, Corros. Sci. **27**, 741 (1987).
12. R. A. Livingston, Environ. Sci. Technol. **25**, 1400 (1991).
13. M. Maar-Stumm, H. Klewe-Nebenius and H.- J. Ache, In: *Wiener Berichte Über Naturwissenschaft In Der Kunst* (A. Vendl, B. Pichler, J. Weber, R. Erlach and G. Banik Eds). 6/7/8, pp. 181-190. ISCA, Hochschule für Angewandte Kunst, Vienna (1989-1991).
14. A. G. Bell, Phil. Mag. **11**, 510 (1881).
15. A. Rosencwaig, Science **181**, 657 (1973).
16. J. C. Murphy L. C. Aamodt and J. W. M. Spicer, In: *Principles and Perspectives of Photothermal and Photoacoustic Phenomena* (A. Mandelis Ed.). pp. 41-94. Elsevier, New York (1992).
17. A. C. Boccara and D. Fournier, In: *Principles and Perspectives of Photothermal and Photoacoustic Phenomena* (A. Mandelis Ed.). pp. 3-42. Elsevier, New York (1992).

18. G. Busse and H. G. Walther, In: *Principles and Perspectives of Photothermal and Photoacoustic Phenomena* (A. Mandelis Ed.). pp. 205-298. Elsevier, New York (1992).

19. G. G. Dolgov-Saveliev, B. A. Knyazev and E. P. Fokin, Zhurnal Prikladnoi Spectroscopii **20**, 805 (1974).

20. A. C. Boccara, D. Fournier and J. Badoz, Appl. Phys. Lett. **36**, 130 (1980).

21. L. C. Aamodt and J. C. Murphy, J. Appl. Phys., **52**, 4903 (1981).

22. M. Munidasa and A. Mandelis, In: *Principles and Perspectives of Photothermal and Photoacoustic Phenomena* (A. Mandelis Ed.). pp. 299-367. Elsevier, New York (1992).

23. J. Rantala, J. Hartikainen and J. Jaarinen, Appl. Phys. A **50**, 465 (1990).

24. We have used a commercially available Mirage monoblock produced by Phototherm Dr. Petry GmbH (Saarbrucken, Germany).

25. J. A. Graham, W. M. Grim and W. G. Frateley, In: *Fourier Transform Infrared Spectroscopy*, Vol.4 (J. R. Ferraro, L. J. Basile, Eds.). pp. 126-134. Academic: Orlando (1985).

26. E. A. Secco, Can. J. Chem. **66**, 329 (1988).

27. N. A. Nielsen, In : *Examination of copper and corrosion product patina from the Statue of Liberty*, Report from E. I. duPont de Nemours and Co. to US National Park Service, Feb. 28 (1981).

28. D. Camuffo, Atmos. Environ. **18**, 2273 (1984).

29. W. C. Keene and J. N. Galloway, Tellus **36B**, 137 (1984).

30. P. K. Kuo, M. J. Lin, C. B. Reyes, L. D. Favro, R. L. Thomas, D. S. Kim, Shu-yi Zhang, L. J. Inglehart, D. Fournier, A. C. Boccara and N. Yacoubi, Can. J. Phys. **64**, 1165 (1986).

31. P. K. Kuo, E. D. Sendler, L. D. Favro and R. L. Thomas, Can. J. Phys. **64**, 1168 (1986).

32. A. Salazar, A. Sanchez-Lavega and J. Fernandez, J. Appl. Phys. **65**, 4150 (1989).

33. A. Salazar, A. Sanchez-Lavega and J. Fernandez, J. Appl. Phys. **69**, 1216 (1991).

34. J. Rantala, J. Jaarinen and P. K. Kuo, Appl. Phys. A **55**, 586 (1992).

35. J. Rantala, L. Wei, P. K. Kuo, J. Jaarinen, M. Luukkala and R. L. Thomas, J. Appl. Phys. **73**, 2714 (1993).

36. S. E. Braslavsky and K. Heihoff, In: *Handbook of Organic Photochemistry* (J. C. Scaiano Ed.), p.327, CRC Press: Boca Raton, Fl (1989).

37. Y. S. Touloukian, R. W. Powell, C. Y. Ho and M. C. Nicolasu, *Thermal Diffusivity*, IFI/Plenum, New York (1973).

38. Y. S. Touloukian, R. W. Powell, C. Y. Ho and P. G. Klemens, *Thermal Conductivity*, IFI/Plenum, New York (1970).

39. Y. S. Touloukian and E. H. Buyco, *Specific Heat*, IFI/Plenum, New York (1970).

40. G. Busse, In: *Optics in Biomedical Sciences* (G. von Bally and P. Greguss, Eds.). pp. 34-56. Springer-Verlag, Berlin (1982).

41. G. Busse, Appl. Phys. Lett., **35**, 759 (1979).

42. R. L. Thomas, J. J. Pouch, Y. H. Wong, L. D. Favro and P. K. Kuo, J. Appl. Phys., **51**, 1152 (1980).

43. We have used the software also supplied by Phototherm Dr. Petry GmbH (Saarbrucken, Germany).

44. J. F. McClelland, Anal. Chem. **55**, 89A (1983).

45. A. Rosencwaig, In : *Photoacoustics and Photoacoustic Spectroscopy* (John Willey and Sons, New York, 1980), Chap. 9, pp. 94-124.

46. E. A. Secco, Can. J. Chem., **66**, 329 (1988).

47. E. A. Secco and G. G. Worth, Can. J. Chem., **65**, 2504 (1987).

48. *The Sadtler Handbook of Inorganic Spectra*, W.W.Simons Ed., Sadtler Res. Lab.Publish., Philadelphia, Pensylvania (1978).

49. E. A. Secco, Can. J. Chem., **66**, 337 (1988).

50. U. Vattulainen and R. Hernberg, Rev. Sci. Instrum., **64**, 1451 (1993).

51. A. Yarai, Y. Fukunaga, K. Sakamoto and T. Nakanishi, Jpn. J. Appl. Phys., **33**, 3251 (1994).